Available online at www.sciencedirect.com
SciVerse ScienceDirect
journal homepage: www.JournalofSurgicalResearch.com

Membranous expression of activated leukocyte cell adhesion molecule contributes to poor prognosis and malignant phenotypes of non–small-cell lung cancer

Futoshi Ishiguro, MD,[a,b] *Hideki Murakami, MD,*[a] *Tetsuya Mizuno, MD,*[a,b] *Makiko Fujii, DDS,*[a] *Yutaka Kondo, MD,*[a] *Noriyasu Usami, MD,*[b] *Tetsuo Taniguchi, MD,*[b] *Kohei Yokoi, MD,*[b] *Hirotaka Osada, MD,*[a,c] *and Yoshitaka Sekido, MD*[a,c,*]

[a] *Division of Molecular Oncology, Aichi Cancer Center Research Institute, Nagoya, Japan*
[b] *Department of Thoracic Surgery, Nagoya University Graduate School of Medicine, Nagoya, Japan*
[c] *Program in Function Construction Medicine, Department of Cancer Genetics, Nagoya University Graduate School of Medicine, Nagoya, Japan*

ARTICLE INFO

Article history:
Received 20 May 2012
Received in revised form
8 August 2012
Accepted 22 August 2012
Available online 7 September 2012

Keywords:
Activated leukocyte cell adhesion molecule
Immunohistochemistry
Non–small-cell lung cancer
Prognosis

ABSTRACT

Background: Activated leukocyte cell adhesion molecule (ALCAM) has been shown to correlate with the prognosis of patients with various types of human malignancies. However, the relationship between ALCAM expression and progression of non–small-cell lung cancer (NSCLC) has not been investigated. This study was designed to clarify the prognostic impact of ALCAM expression of NSCLC cells.

Materials and methods: The study population consisted of 147 NSCLC patients who underwent complete resection. We performed immunohistochemical staining for ALCAM expression and correlated this to the clinicopathologic parameters and patient survival. The ALCAM expression in NSCLC cell lines was analyzed using quantitative reverse transcription–polymerase chain reaction and Western blot analyses. ALCAM knockdown in NSCLC cell lines was performed with lentivirus-mediated short hairpin RNA transduction.

Results: Positive membranous and cytoplasmic ALCAM expressions were detected in 66 (44.9%) and 57 (38.8%) patients, respectively. A significant association of high membranous ALCAM expression with shortened overall survival (OS) was found ($P = 0.009$). However, patients with cytoplasmic staining of ALCAM showed no significantly shortened OS ($P = 0.723$). Multivariate analyses showed that membranous expression was adverse prognostic factors for OS (hazard ratio, 2.11; $P = 0.046$). ALCAM knockdown with short hairpin RNA suppressed cell migration and invasion of NSCLC cell lines *in vitro*.

Conclusions: Strong membranous ALCAM expression is associated with a poor prognosis in patients with resected NSCLC, and overexpression of ALCAM causes malignant phenotypes of NSCLC.

1. Introduction

Lung cancer is the most common cause of death from cancer [1]. Non–small-cell lung cancer (NSCLC) accounts for approximately 85% of all lung cancers. Despite the progress of treatment modalities in the past decade, the 5-y survival rate of NSCLC patients with surgical treatment remains only 69.6% [2]. Better understanding of the molecular features of NSCLC

* *Corresponding author.* Division of Molecular Oncology, Aichi Cancer Center Research Institute, 1-1 Kanokoden, Chikusa-ku, Nagoya, Aichi 464-8681, Japan. Tel.: +81 52 764 2983; fax: +81 52 764 2993.
E-mail address: ysekido@aichi-cc.jp (Y. Sekido).
0022-4804/$ – see front matter © 2013 Elsevier Inc. All rights reserved.
http://dx.doi.org/10.1016/j.jss.2012.08.044

would help to identify an effective therapeutic target of this malignant tumor. Regarding the prognostic indicators of NSCLC, the pathologic stage has been consistently shown to be the best predictor for prognosis [3]. Although other clinical factors including gender, age, and smoking history have also been shown to be a possible prognostic factor for NSCLC patients, further development of novel biological or genetic factors would become an aid for predicting NSCLC patient prognosis more precisely.

Activated leukocyte cell adhesion molecule (ALCAM or CD166) belongs to the immunoglobulin superfamily, which mediates both heterophilic (ALCAM–CD6) and homophilic (ALCAM–ALCAM) cell–cell interactions [4]. ALCAM has been reported to promote cell migration [5,6] and angiogenesis [7] *in vitro* and be involved in invasion and metastases of primary tumors [8,9]. Since its discovery, ALCAM has also been shown as a prognostic marker in colorectal cancer [10], gastric cancer [11], and various types of malignant tumors [12–17]. However, the relationship between the ALCAM expression and malignant phenotypes of NSCLC has not been reported.

The aim of this study was to evaluate the prognostic significance of ALCAM in NSCLC, which has not been explored to date. We investigated the expression of ALCAM in a cohort of clinically characterized NSCLC by immunohistochemistry (IHC) and correlated that with clinicopathologic features. Moreover, we knocked down ALCAM in NSCLC cell lines to evaluate its effects on malignant phenotypes of NSCLC *in vitro*.

Table 1 – Clinicopathologic characteristics of 147 patients with NSCLC.

Variables	Number of patients (*n*)	%
Total, N	147	
Age (y)		
Median (range)	68 (35–84)	
Sex		
Female	48	32.7
Male	99	67.3
Smoking status		
Pack-years ≥20	58	39.5
<20	89	60.5
CEA (ng/mL)*		
≥5	88	62.4
<5	53	37.6
Histology		
Adenocarcinoma	101	68.7
Squamous cell carcinoma	40	27.2
Other	6	4.1
Pathologic stage		
I	93	63.3
II	33	22.4
III	21	14.3
Operation		
Lobectomy	122	83.0
Bilobectomy/extended lobectomy	8	5.4
Lobectomy with adjacent organ resection	9	6.2
Pneumonectomy	8	5.4

* Serum CEA levels were not measured in six patients.

2. Materials and methods

2.1. Patient samples

From January 2004 through June 2006, 147 patients had complete resection by lobectomy or pneumonectomy with mediastinal lymph node dissection for primary NSCLC at the Nagoya University Hospital. The clinicopathologic features of patients were summarized in Table 1. Overall survival (OS) was measured from the date of surgery until death or the final date of the follow-up (March 31, 2011). The median length of follow-up for all the patients was 55 mo (range, 4–78 mo), and the median length of follow-up for surviving patients was 61 mo (range, 33–78 mo). Tumors were pathologically staged based on the 7th Edition of the TNM Classification for Lung and Pleural Tumors [18]. The histologic subtype was classified according to the World Health Organization guidelines [19]. The study was approved by the institutional review boards. Written informed consent was obtained before the resection from all the patients regarding tissue sampling.

2.2. IHC analysis

IHC analysis was carried out on formalin-fixed paraffin-embedded tissue sections of tumor samples. Sections (4-μm thick) were deparaffinized in xylene and rehydrated in increasing concentrations of ethanol. The antigens were retrieved by 45-min heating at 98°C in 0.5% Immunosaver (Nisshin EM, Tokyo, Japan) in a water bath. After blocking the endogenous peroxidase activity with 3% aqueous H_2O_2 solution for 15 min, the slides were incubated in blocking solution for 15 min, followed by 1-h incubation at room temperature (RT) with a primary mouse monoclonal anti-ALCAM antibody (clone MOG/07; NovoCastra, Newcastle, UK) at a 1:200 dilution. After washing, the slides were incubated with a biotinylated secondary antibody for 15 min at RT and allowed to react for 15 min with the streptoavidin–peroxidase reagent using an Ultra-tech Kit (Beckman Coulter, Marseille, France). The 3,3′-diaminobenzidine tetrahydrochloride Liquid System (DakoCytomation, Glostrup, Denmark) was used to detect immunostaining. Normal mouse immunoglobulin or omission of the primary antibody served as negative controls (Fig. 1F).

2.3. Positive criterion for IHC staining

ALCAM showed membranous and cytoplasmic staining patterns. The intensity of each membranous and cytoplasmic staining was scored for positivity as follows: 0, no staining or faint staining in <10% of tumor cells; 1+, faint staining in >10% of tumor cells; 2+, weak or moderate staining in >10% of tumor cells; and 3+, >10% of strong staining. Zero or 1+ staining intensity was considered ALCAM negative, and 2+ or 3+ staining intensity was considered positive as reported previously [10,11,16]. Two independent researchers (F.I. and H.M.) blinded to patient characteristics, and outcome evaluated the slides. All cases with discrepant evaluations were discussed during observation with the same microscope, and a consensus was reached.

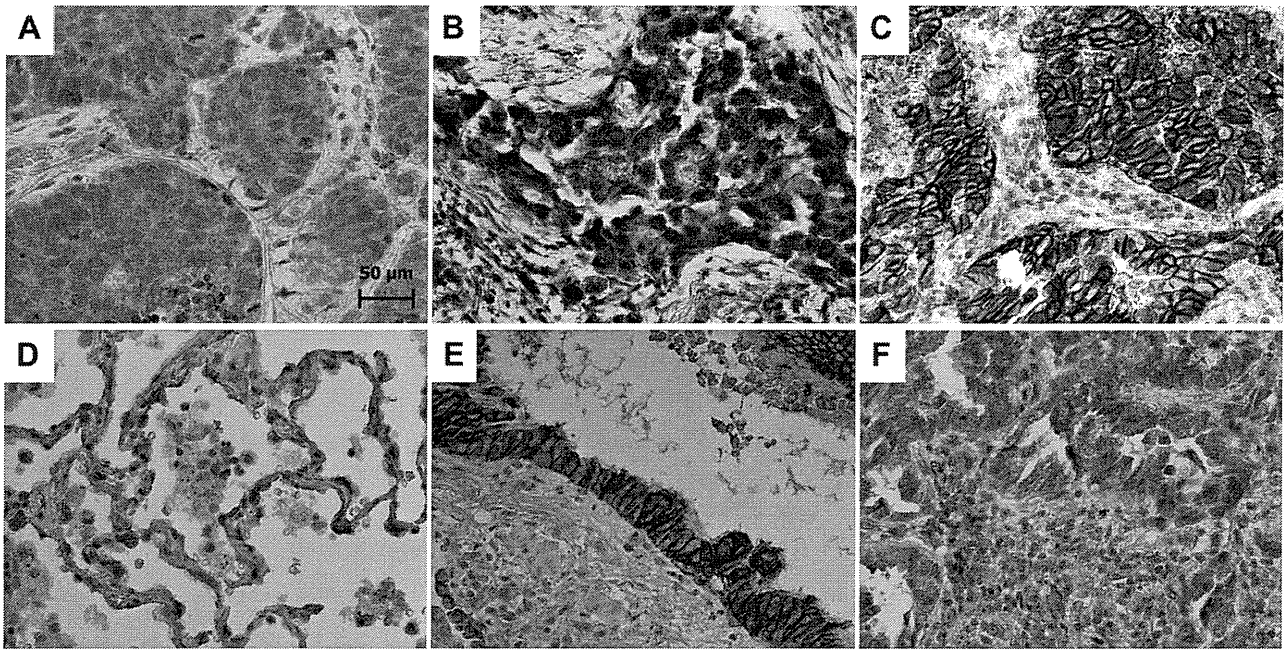

Fig. 1 – IHC analysis of ALCAM in NSCLC and normal lung tissues. (A) NSCLC displaying an ALCAM intensity of 0. (B) NSCLC displaying a cytoplasmic intensity of 3+. (C) NSCLC displaying membranous intensity of 3+. (D) Alveolar epithelial cells with a cytoplasmic ALCAM intensity of 1+. (E) Bronchoepithelial cells with strong membranous immunoreactivity of 3+, which served as a positive control of immunostainings. (F) The same specimen (C) was stained with the omission of primary antibody, which served as negative control. Original magnification, ×400.

2.4. *Cell lines*

The human NSCLC cell lines HCC78 and HCC193 were the kind gift of Dr Adi F. Gazdar. A549, H2228, H596, and NCI-H23 cell lines were purchased from the American Type Culture Collection (ATCC, Rockville, MD). VMRC-LCD was obtained from the Japanese Collection of Research Bioresources (Osaka, Japan). A human bronchial epithelial cell line (BEAS-2B) transformed with SV40 virus was purchased from the ATCC. All the NSCLC cell lines were cultured in RPMI-1640 medium supplemented with 10% fetal calf serum and 1× antibiotic–antimycotic (Invitrogen, Carlsbad, CA) at 37°C in a humidified incubator with 5% CO_2. BEAS-2B was cultured according to the ATCC instructions.

2.5. *Preparation of RNA*

Total RNA was prepared using RNeasy Plus RNA extraction kit (Qiagen, Tokyo, Japan) according to the manufacturer's protocol. Random-primed first-strand complementary DNA was synthesized from 1.0 μg of total RNA using Superscript II according to the manufacturer's instructions (Invitrogen).

2.6. *Quantitative reverse transcription–polymerase chain reaction*

Quantitative reverse transcription–polymerase chain reaction was performed using first-strand complementary DNA with Power SYBR Green PCR Master (Applied Biosystems, Foster City, CA). The amplification was carried out with an ABI 7500 Real-Time PCR system (Applied Biosystems) according to the manufacturer's instructions. *Glyceraldehyde-3-phosphate dehydrogenase* served as an internal control; the expression levels of *ALCAM* in each of the samples were normalized on the basis of the corresponding *glyceraldehyde-3-phosphate dehydrogenase* content and recorded as relative expression levels.

2.7. *Antibodies*

Mouse anti-ALCAM antibody (clone MOG/07 and SNCL-CD166) for Western blot and IHC analyses was purchased from Novocastra. Mouse anti-ALCAM (clone 3A6 and 559260) for immunofluorescence was purchased from BD Bioscience Discovery Labware (Bedford, MA) and mouse anti-β-actin (clone AC74) was from Sigma (St Louis, MO). Rabbit anti-β-catenin antibody (sc-7199) was purchased from Santa Cruz Biotechnology (Santa Cruz, CA).

2.8. *Western blot analysis*

The preparation of total cell lysates and Western blotting were carried out as described previously [20]. In brief, cells growing confluently were rinsed twice with phosphate-buffered saline, lysed in sodium dodecyl sulfate (SDS) sample buffer (62.5 mM Tris, pH 6.8, 2% SDS, 2% 2-mercaptoethanol, and 10% glycerol), and homogenized. Total cell lysate (30 μg) was subjected to SDS–polyacrylamide gel electrophoresis and transferred to Immobilon-P polyvinylidene difluoride membranes (Millipore, Bedford, MA). After blocking with 3% nonfat dry milk, the filters were incubated with the primary antibody, washed with

phosphate-buffered saline, reacted with the secondary antibody, and then detected with enhanced chemiluminescence (Amersham Bioscience, Buckinghamshire, UK).

2.9. *Immunofluorescent microscopic analysis*

Cells were fixed, permeabilized, and incubated with a primary antibody (anti-ALCAM antibody, 2.5 μg/mL and anti-β-catenin antibody, 0.4 μg/mL) for 1 h at RT, followed by incubation with Alexa Fluor 488- or Alexa Fluor 564-conjugated secondary antibodies at RT. Nuclear staining was carried out with 4′, 6-diamidino-2-phenylindole after incubation with secondary antibody. Microscopic observation was carried out using a confocal laser scanning system (LSM510; Carl Zeiss Micro-Imaging GmbH, Jena, Germany) at ×63 magnification, as described previously [21].

2.10. *Construction of RNA interference vectors*

Complementary short hairpin sequence was cloned into pLentiLox3.7 [20] under the control of a U6 promoter and transfected into HEK293FT cells along with the vectors of VSVG, RSV-Rev, and pMDLg-pRPE to generate lentiviruses that transcribe short hairpin RNA. A short hairpin oligonucleotide was designed for sequence within the ALCAM open reading frame (ALCAM-Sh, 5′-GAGGAATCTCCTTATATTA-3′). A control vector, ALCAM-Scr (5′-GTTTACCACGGAATATTAT-3′), was constructed using oligonucleotide with scrambled sequence for ALCAM-Sh. The efficacy of each virus was tested by immunoblotting of whole-cell lysates 96 h after infecting cells at the multiplicity of infection of 10.

2.11. *Cell migration and invasion assays*

Cell migration and invasion potential were measured by *in vitro* Boyden chamber assays (BD Bioscience Discovery Labware) according to the manufacturer's protocol. Briefly, NSCLC cells (5×10^4 for transwell migration assay and 1×10^5 for Matrigel invasion assay) in 0.5 mL of serum-free RPMI-1640 medium were added to the upper wells of Matrigel-uncoated or Matrigel-coated Boyden chambers with 8-μm pore membrane. The bottom chambers were filled with 5% fetal calf serum–containing medium as a chemoattractant. After 22-h incubation, noninvasive cells were removed by scrubbing with a cotton swab. Cells that migrated through the membrane and stuck to the lower surface of the membrane were fixed stained using Diff-Quick stain (Sysmex, Kobe, Japan). Values for migration and invasion were obtained by counting five predetermined fields per membrane at ×100 magnifications, representing the average of three independent experiments.

2.12. *Statistical analysis*

For statistical analysis, chi-square or Fisher exact test was used to assess the significance of associations between the expression of ALCAM and clinicopathologic parameters. Continuous variables were compared using unpaired *t*-test. The Kaplan–Meier method was used to estimate OS curves, and the survival differences were analyzed by the log-rank test. A multivariate analysis was performed using the Cox proportional hazard model to study the effects of variables on survival. The *P* values of all statistical tests were two sided, and the differences were considered significant at *P* values <0.05. All analyses were performed using StatView software (version 5; SAS Institute Inc, Cary, NC).

3. Results

3.1. *IHC analysis of ALCAM in NSCLCs and normal lung tissues*

ALCAM displayed a differential subcellular expression patterns, that is, membranous and cytoplasmic staining (Fig. 1A–C). Positive membranous staining was seen in 66 (44.9%) patients and positive cytoplasmic staining in 57 (38.8%) patients (Table 2). These ALCAM staining patterns were in concordance with IHC patterns in the Human Protein Atlas database (www.proteinatlas.org). Apart from NSCLC cells, alveolar epithelial cells (Fig. 1D), normal mesothelium, and reactive mesothelial cells showed ALCAM intensity of 1+. Bronchoepithelial cells (Fig. 1E), macrophages, and neural cells showed a staining intensity of 3+ in a membranous fashion. We repeated IHC with two different antibodies of ALCAM, primary mouse monoclonal anti-ALCAM antibody (clone MOG/07; NovoCastra) and primary rabbit polyclonal anti-ALCAM antibody (Atlas Antibody AB, Stockholm, Sweden). The expression patterns were identical between the two different antibodies. We then used only the monoclonal antibody for IHC evaluation because it has also been successfully approved in previous reports [10–13,15].

3.2. *ALCAM expression by IHC in correlation with clinicopathologic parameters and prognosis*

We investigated the relationship between the clinicopathologic characteristic of NSCLC and ALCAM IHC staining. No correlations between membranous or cytoplasmic immunoreactivity and clinicopathologic variables were found (Table 3). Figure 2 showed OS stratified by subcellular

Table 2 – Membranous and cytoplasmic staining status of ALCAM.

Cytoplasmic staining	Score	Membranous staining				Total
		Negative		Positive		
		0	1+	2+	3+	
Negative	0	21	7	5	0	33
	1+	11	8	30	8	57
Positive	2+	18	13	18	2	51*
	3+	1	2	3	0	6*
Total		51	30	56†	10†	147

Membranous and cytoplasmic positivities were evaluated separately.
* A total of 57 (38.8%) patients showed cytoplasmic expression.
† A total of 66 (44.9%) patients showed membranous expression.

Table 3 – Patient characteristics stratified ALCAM IHC staining status.

Variables	Number of patients	A			B		
		ALCAM IHC		P value	ALCAM IHC		P value
		Membranous positive	Membranous negative		Cytoplasmic positive	Cytoplasmic negative	
Total	147	66	81		57	90	
Age (y)							
Median (range)		70 (35–84)	67 (40–81)	0.113*	67 (40–80)	69 (35–84)	0.095*
Sex							
Female	48	24	24	0.387†	20	28	0.616†
Male	99	42	57		37	62	
Smoking status							
Pack-years ≥20	58	29	29	0.315†	23	35	0.860†
<20	89	37	52		34	55	
CEA (ng/mL)‡							
≥5	88	33	55	0.118†	35	53	0.642†
<5	53	27	26		19	34	
Histology							
Adenocarcinoma	101	48	53	0.315†	46	55	0.200†
Squamous cell carcinoma	40	17	23		10	30	
Other	6	1	5		1	5	
Pathologic stage							
I	93	42	51	0.979†	38	55	0.093†
II	33	15	18		8	25	
III	21	9	12		11	10	

* Fisher exact or chi-square test.
† Mann–Whitney *U*-test.
‡ Serum CEA levels were not measured in six patients.

expression patterns of ALCAM. Patients with membranous ALCAM expression showed a significantly shortened OS compared with those tumors showed negative expression ($P = 0.009$). The 5-y survival probabilities were 64.5% for the membranous-positive group and 82.0% for the membranous-negative group (Fig. 2A). In contrast, patients whose tumors showed positive cytoplasmic staining of ALCAM did not have a significant survival difference compared with ALCAM cytoplasmic-negative group ($P = 0.723$) (Fig. 2B).

3.3. *Prognostic values of ALCAM expression*

We analyzed the impact of all variables on OS. Univariate analysis showed a significant prognostic difference with

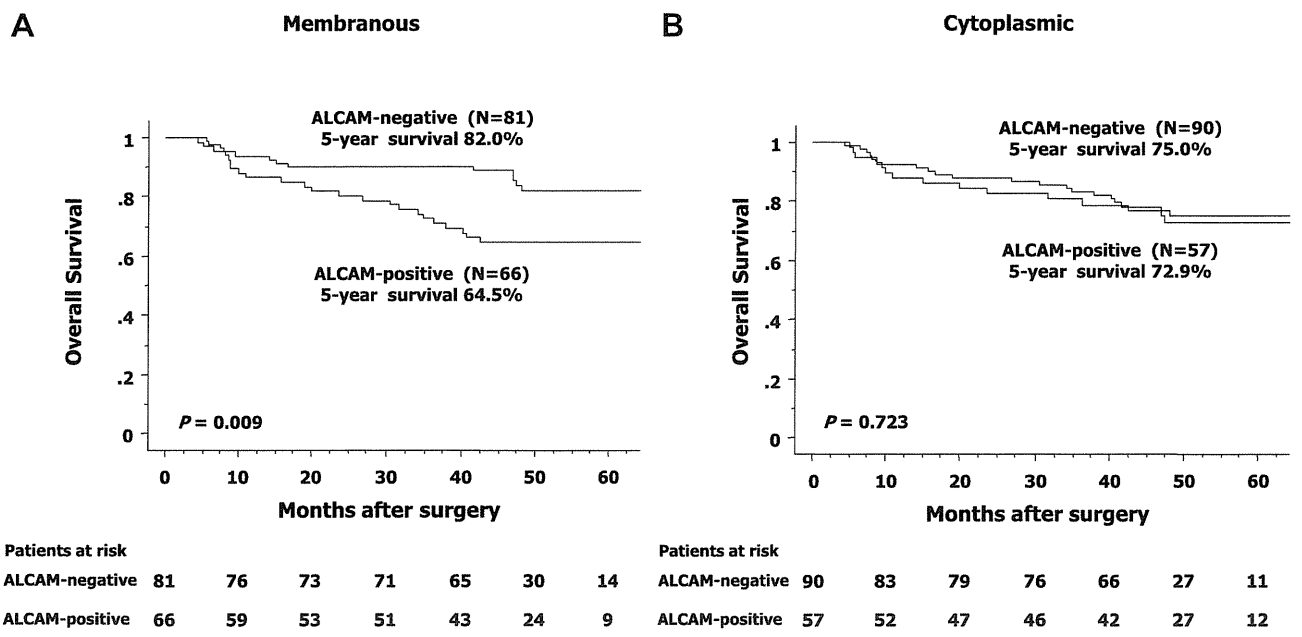

Fig. 2 – Kaplan–Meier survival analysis stratified by positive or negative ALCAM IHC staining according to (A) membranous and (B) cytoplasmic staining.

age, sex, smoking status, serum Carcinoembryonic antigen, histology, pathologic stage, and ALCAM membranous expression (Table 4). As shown in Table 5, multivariate analysis confirmed membranous ALCAM expression as an independent negative prognostic factor (hazard ratio, 2.11; 95% confidence interval, 1.01–4.42, $P = 0.046$). Among the remaining variables, age, sex, serum CEA, and pathologic stage were significant in our patient cohort (Table 5).

3.4. *ALCAM expression in NSCLC cell lines*

We next examined the expression status of ALCAM with quantitative reverse transcription–polymerase chain reaction and Western blot analyses in seven NSCLC cell lines and an immortalized bronchial epithelial cell line, BEAS-2B. Consistent with the result of positive ALCAM staining of bronchoepithelial cells with IHC (Fig. 1E), we found that BEAS-2B also expressed ALCAM. Among the seven NSCLC cell lines, we considered six cell lines expressed relatively high ALCAM messenger RNA (Fig. 3A). Figure 3B showed that ALCAM protein levels determined by Western blot analysis showed a good correlation with messenger RNA in most cell lines. We also performed the immunocytochemical analysis using HCC193 and H596 cells and observed strong signals at cell–cell interaction regions (Fig. 3C).

3.5. *Inhibition of ALCAM suppressed migration and invasion of mesothelioma cells*

To determine whether ALCAM plays a possible role in NSCLC progression, we investigated whether inhibition of ALCAM suppresses malignant phenotypes of NSCLC cells. We selected HCC193 and H596 as representative cell lines with high ALCAM protein expression. We synthesized ALCAM short hairpin RNA constructs and transduced into these cell lines. Efficient depletion of ALCAM expression was confirmed by Western blot analysis (Fig. 4A). ALCAM-depleted cells showed weaker migration and invasion ability compared with control cells (Fig. 4B and C). However, we did not detect the inhibitory effect on cell proliferation by ALCAM knockdown (data not shown).

Table 4 – Univariate analysis of factors associated with patient survival.

Variables	HR	95% CI	P value
Age (continuous)	1.06	1.02–1.11	0.009
Sex			
Female/male	6.37	1.96–20.83	0.002
Smoking status			
Pack-years ≥20/<20	3.10	1.36–7.09	0.007
CEA (ng/mL)*			
≥5/<5	3.53	1.74–7.19	0.001
Histology			
Adenocarcinoma/other	2.18	1.13–4.18	0.020
Pathologic stage			
I/II + III	3.82	1.93–7.52	0.001
ALCAM membranous staining			
Negative/positive	3.56	1.76–7.19	0.012
ALCAM cytoplasmic staining			
Negative/positive	1.13	0.58–2.19	0.723

CI = confidence interval; HR = hazard ratio.
* Serum CEA levels were not measured in six patients.

Table 5 – Multivariate analysis of factors associated with patient survival.

Variables	HR	95% CI	P value
Age (continuous)	1.05	1.00–1.10	0.039
Sex			
Female/male	7.41	1.56–29.52	0.012
Smoking status			
Pack-years ≥20/<20	1.44	0.46–4.48	0.530
CEA (ng/mL)*			
≥5/<5	2.33	1.12–4.87	0.024
Histology			
Adenocarcinoma/others	1.09	0.50–2.37	0.828
Pathologic stage			
I/II + III	3.69	1.75–7.75	0.001
ALCAM membranous staining			
Negative/positive	2.11	1.01–4.42	0.046

CI = confidence interval; HR = hazard ratio.
* Serum CEA levels were not measured in six patients.

4. Discussion

To our knowledge, this is the first report of a retrospective study designed to clarify the possible impact of ALCAM expression on patient outcome in completely surgically resected NSCLC. Among 147 NSCLC patients, 66 (44.9%) tumors showed positive membranous ALCAM staining and 57 (38.8%) showed cytoplasmic ALCAM staining with IHC analysis. We found that the increased membranous, but not cytoplasmic, overexpression of ALCAM was associated with poor prognosis of NSCLC patients.

The association of ALCAM with disease progression in human malignancies has been first suggested in malignant melanoma [9]. Subsequently, as a poor prognostic factor, ALCAM has also been indicated in various types of human malignancies [10–17]. As for its expression in NSCLC, ALCAM was detected as one of the elevated cancer-specific molecules in malignant pleural effusion of NSCLC patients with shotgun mass spectrometry [22]. The levels of ALCAM expression in pleural effusion were correlated with the signal intensities of the primary tumors that were detected with IHC, and the membranous expression of ALCAM was also confirmed in the tumor cells. Recently, ALCAM has been shown to be a cell surface marker, which enriches for cancer stem cells in NSCLC [23] and also to be one of the new potential biomarkers for diagnosis and prognosis of lung cancer [24]. We hypothesized that ALCAM might have a possible impact on NSCLC progression and determined to investigate the correlation between ALCAM expression and NSCLC patient survival.

In this study, we identified two types of ALCAM expression patterns, membranous and cytoplasmic, in NSCLC tumors as reported in other types of malignancies [9–17]. We found that the membranous expression of ALCAM was of prognostic value, whereas the cytoplasmic expression was not. Thus, our

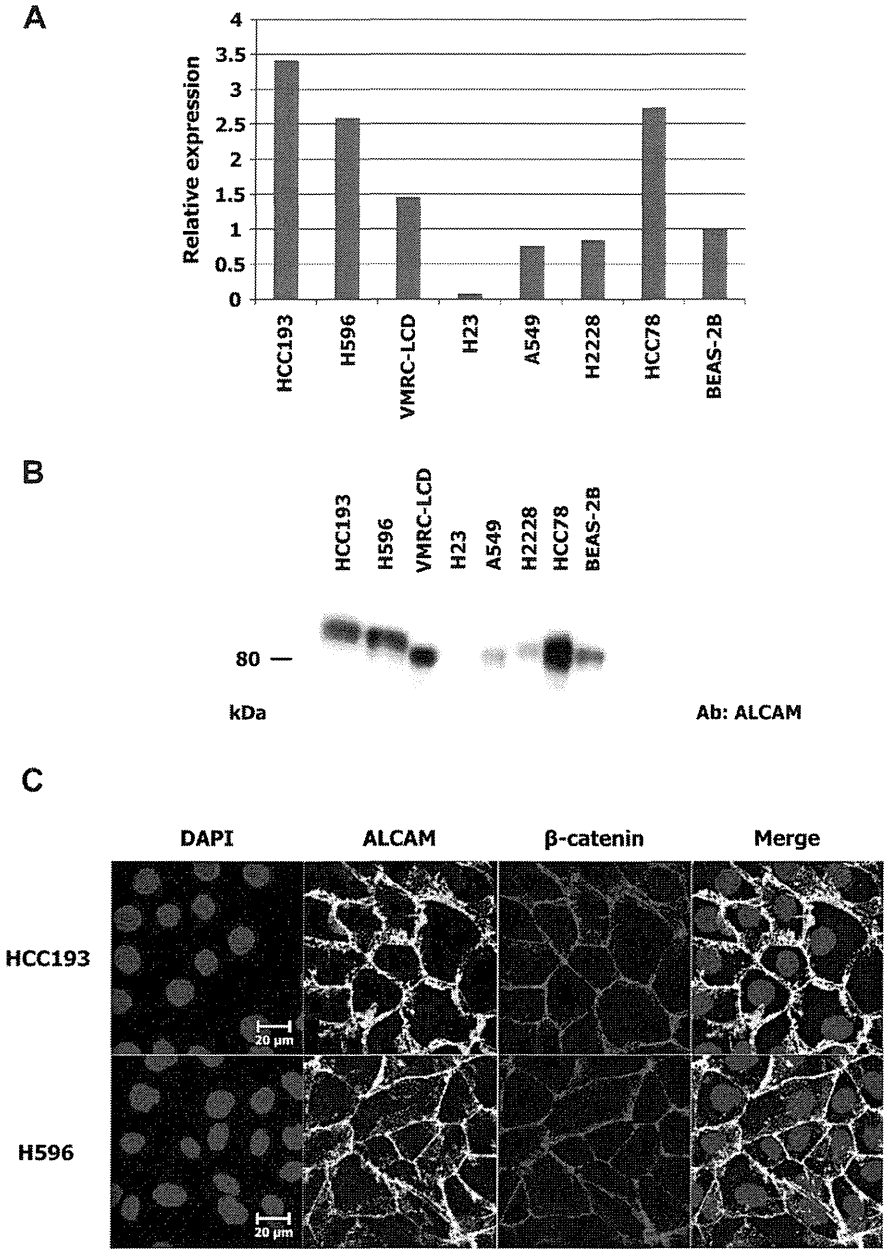

Fig. 3 – The expression of ALCAM in NSCLC cell lines. (A) Quantitative reverse transcription–polymerase chain reaction analysis of ALCAM in seven NSCLC cell lines and one immortalized bronchial epithelial cells, BEAS-2B. The relative expression of BEAS-2B was arbitrarily set as 1.0. (B) Western blot analysis of ALCAM in seven NSCLC cell lines. The expression of β-actin was used as the control. (C) Immunocytochemical analysis. Strong membranous signals of ALCAM were observed in HCC193 and H596 cells. β-Catenin staining was used as the marker of the cell–cell interaction region.

findings suggested that membranous expression of ALCAM in NSCLC cells was also associated with a worse prognosis of patients with NSCLC, similarly to other types of tumors, including melanoma [9], colorectal cancer [10], and gastric cancer [11]. In contrast, the association with an unfavorable prognosis of cytoplasmic ALCAM staining was also suggested in breast cancer [13] and ovarian cancer [15], although we did not confirm this in the present study. Thus, the previous and our studies may indicate that the evaluation of the prognostic impact of ALCAM expression in tumor cells should be considered for each type of tumor based on subcellular localization and expression levels of ALCAM.

With respect to subcellular localization of ALCAM, Tomita *et al.* investigated the relationship between ALCAM and cytoskeleton. They found that loss of α-catenin, which is involved in actin filament network via actin-binding activity, led to cytoplasmic localization of ALCAM [25]. They concluded that α-catenin played a significant role in the cell surface localization of ALCAM and its membranous localization by α-catenin, thereby enhanced a physiological function of ALCAM. In this regard, it should be noted that membranous ALCAM might be a more activated form that can interact with extracellular components because ALCAM, which consists of five extracellular domains, seems to fulfill its original function

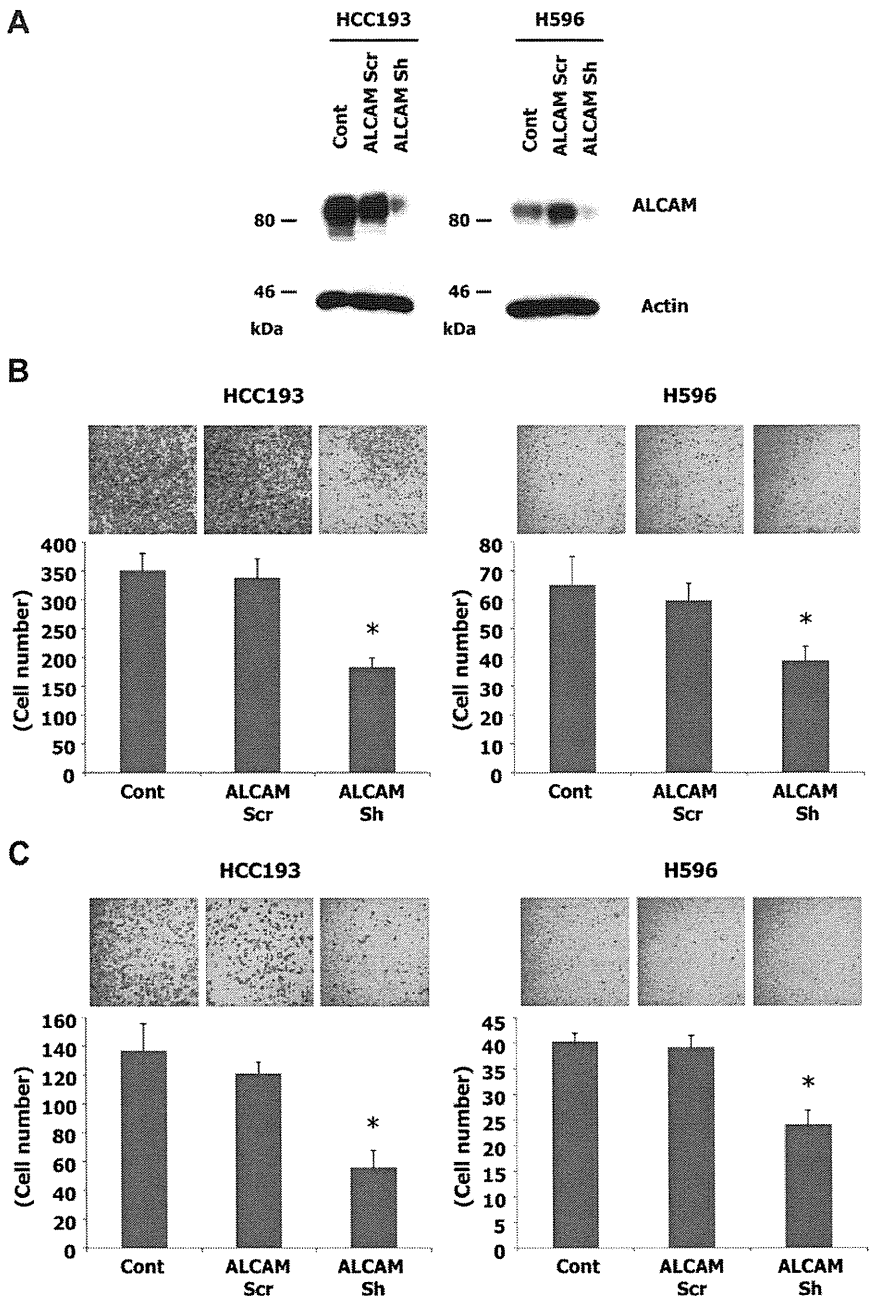

Fig. 4 – Lentiviral short hairpin RNA–mediated ALCAM knockdown in two NSCLC cell lines, HCC193 and H596. (A) Western blot analysis demonstrates the efficiency of ALCAM knockdown. The ALCAM-Sh vectors, ALCAM Sh, showed effective suppression of the level of ALCAM protein, whereas the control vectors, ALCAM Scr, showed no downregulation. Cells were lysed 96 h after infection. (B) ALCAM knockdown inhibited migration of two NSCLC cell lines. (C) ALCAM knockdown inhibited invasion of two NSCLC cell lines. The results of the triplicate experiments are presented. Columns, mean and bars, standard deviation. *P < 0.05 *versus* control.

as its homophilic interaction. However, it also remains to determine whether cytoplasmic ALCAM may have any other cancer-promoting function in cells including lung cancer.

ALCAM-mediated cell–cell adhesion was reported to promote matrix metalloprotease (MMP) activation in malignant melanoma cell lines [26]. They showed that ALCAM was involved in a regulatory role of MMP activity, which promotes proteolysis related to cancer invasion. Overexpression of MMPs was also described in resected NSCLC [27], and we found ALCAM promoted cell invasion *in vitro*. Taken together, these findings might imply that the positive role of ALCAM that leads to progression and metastases of NSCLC might be coupled to the increased activity of MMP.

In conclusion, our study suggested that membranous ALCAM expression was associated with the poor survival of patients with NSCLC. It also suggested that membranous ALCAM expression enhanced motility and invasion capacity of NSCLC cells *in vitro*. In this regard, patients whose tumor

has proved to be positive for membranous ALCAM expression, even if they have early-stage NSCLC, may well be considered for more careful management including adjuvant chemotherapy to improve their estimated poor outcome. Further studies are warranted to define the mechanism of ALCAM expression, which might also provide new insights into the better understanding of cell adhesion and progressive invasiveness of NSCLC cells.

Acknowledgment

The authors thank Mika Yamamoto and Tsutsumi Koike for their excellent technical assistance.

Sources of funding: This work is supported by a grant-in-aid for Scientific Research (B) from Japan Society for the Promotion of Science (22300338), a grant-in-aid for Third-Term Comprehensive Control Research for Cancer from the Ministry of Health, Labor and Welfare of Japan, and the Takeda Science Foundation.

Disclosures: None declared.

REFERENCES

[1] Jemal A, Bray F, Center MM, et al. Global cancer statistics. CA Cancer J Clin 2011;61:69.
[2] Sawabata N, Miyaoka E, Asamura H, et al. Japanese lung cancer registry study of 11,663 surgical cases in 2004: demographic and prognosis changes over decade. J Thorac Oncol 2011;6:1229.
[3] Oldenhuis CN, Oosting SF, Gietema JA, et al. Prognostic versus predictive value of biomarkers in oncology. Eur J Cancer 2008;44:946.
[4] van Kempen LC, Nelissen JM, Degen WG, et al. Molecular basis for the homophilic activated leukocyte cell adhesion molecule (ALCAM)-ALCAM interaction. J Biol Chem 2001;276:25783.
[5] van Kilsdonk JW, Wilting RH, Bergers M, et al. Attenuation of melanoma invasion by a secreted variant of activated leukocyte cell adhesion molecule. Cancer Res 2008;68:3671.
[6] Heffron DS, Golden JA. DM-GRASP is necessary for nonradial cell migration during chick diencephalic development. J Neurosci 2000;20:2287.
[7] Ikeda K, Quertermous T. Molecular isolation and characterization of a soluble isoform of activated leukocyte cell adhesion molecule that modulates endothelial cell function. J Biol Chem 2004;279:55315.
[8] Weidle UH, Eggle D, Klostermann S, Swart GW. ALCAM/CD166: cancer-related issues. Cancer Genomics Proteomics 2010;7:231.
[9] van Kempen LC, van den Oord JJ, van Muijen GN, et al. Activated leukocyte cell adhesion molecule/CD166, a marker of tumor progression in primary malignant melanoma of the skin. Am J Pathol 2000;156:769.
[10] Weichert W, Knösel T, Bellach J, et al. ALCAM/CD166 is overexpressed in colorectal carcinoma and correlates with shortened patient survival. J Clin Pathol 2004;57:1160.
[11] Ishigami S, Ueno S, Arigami T, et al. Clinical implication of CD166 expression in gastric cancer. J Surg Oncol 2011; 103:57.
[12] Kahlert C, Weber H, Mogler C, et al. Increased expression of ALCAM/CD166 in pancreatic cancer is an independent prognostic marker for poor survival and early tumour relapse. Br J Cancer 2009;101:457.
[13] King JA, Ofori-Acquah SF, Stevens T, et al. Activated leukocyte cell adhesion molecule in breast cancer: prognostic indicator. Breast Cancer Res 2004;6:478.
[14] Tomita K, van Bokhoven A, Jansen CF, et al. Activated leukocyte cell adhesion molecule (ALCAM) expression is associated with poor prognosis for bladder cancer patients. UroOncology 2003;3:121.
[15] Mezzanzanica D, Fabbi M, Bagnoli M, et al. Subcellular localization of activated leukocyte cell adhesion molecule is a molecular predictor of survival in ovarian carcinoma patients. Clin Cancer Res 2008;14:1726.
[16] Verma A, Shukla NK, Deo SV, et al. MEMD/ALCAM: a potential marker for tumor invasion and nodal metastasis in esophageal squamous cell carcinoma. Oncology 2005; 68:462.
[17] Sawhney M, Matta A, Macha MA, et al. Cytoplasmic accumulation of activated leukocyte cell adhesion molecule is a predictor of disease progression and reduced survival in oral cancer patients. Int J Cancer 2009;124:2098.
[18] Goldstraw P. Staging manual in thoracic oncology. Denver: IASLC; 2009.
[19] Travis WD, Brambilla E, Muller-Hermelink H, et al. Pathology and genetics of tumours of the lung, pleura, thymus and heart. Lyon: IARC Press; 2004.
[20] Kawaguchi K, Murakami H, Taniguchi T, et al. Combined inhibition of MET and EGFR suppresses proliferation of malignant mesothelioma cells. Carcinogenesis 2009;30:1097.
[21] Murakami H, Mizuno T, Taniguchi T, et al. LATS2 is a tumor suppressor gene of malignant mesothelioma. Cancer Res 2011;71:873.
[22] Soltermann A, Ossola R, Kilgus-Hawelski S, et al. N-glycoprotein profiling of lung adenocarcinoma pleural effusions by shotgun proteomics. Cancer 2008;114:124.
[23] Zhang WC, Shyh-Chang N, Yang H, et al. Glycine decarboxylase activity drives non-small cell lung cancer tumor-initiating cells and tumorigenesis. Cell 2012;148:259.
[24] Sudhir PR, Chen CH, Kumari MP, et al. Label-free quantitative proteomics and N-glycoproteomics analysis of KRAS-activated human bronchial epithelial cells. Mol Cell Proteomics; 2012 Jul 3 [Epub ahead of print].
[25] Tomita K, van Bokhoven A, Jansen CF, et al. Coordinate recruitment of E-cadherin and ALCAM to cell-cell contacts by alpha-catenin. Biochem Biophys Res Commun 2000;267:870.
[26] Lunter PC, van Kilsdonk JW, van Beek H, et al. Activated leukocyte cell adhesion molecule (ALCAM/CD166/MEMD), a novel actor in invasive growth, controls matrix metalloproteinase activity. Cancer Res 2005;65:8801.
[27] Cox G, Jones JL, O'Byrne KJ. Matrix metalloproteinase 9 and the epidermal growth factor signal pathway in operable non-small cell lung cancer. Clin Cancer Res 2000;6:2349.

The EMBO Journal (2012) 31, 481–493 | © 2012 European Molecular Biology Organization | All Rights Reserved 0261-4189/12
www.embojournal.org

THE EMBO JOURNAL

MYBPH, a transcriptional target of TTF-1, inhibits ROCK1, and reduces cell motility and metastasis

Yasuyuki Hosono[1,2], Tomoya Yamaguchi[1], Eri Mizutani[1], Kiyoshi Yanagisawa[1,3], Chinatsu Arima[1], Shuta Tomida[1], Yukako Shimada[1], Michiyo Hiraoka[1], Seiichi Kato[1], Kohei Yokoi[2], Motoshi Suzuki[1] and Takashi Takahashi[1,*]

[1]Division of Molecular Carcinogenesis, Center for Neurological Diseases and Cancer, Nagoya University Graduate School of Medicine, Nagoya, Japan, [2]Department of Thoracic Surgery, Nagoya University Graduate School of Medicine, Nagoya, Japan and [3]Institute for Advanced Research, Nagoya University, Nagoya, Japan

Cell migration driven by actomyosin filament assembly is a critical step in tumour invasion and metastasis. Herein, we report identification of *myosin binding protein H* (*MYBPH*) as a transcriptional target of *TTF-1* (also known as *NKX2-1 and TITF1*), a master regulator of lung development that also plays a role as a lineage-survival oncogene in lung adenocarcinoma development. MYBPH inhibited assembly competence-conferring phosphorylation of the myosin regulatory light chain (RLC) as well as activating phosphorylation of LIM domain kinase (LIMK), unexpectedly through its direct physical interaction with Rho kinase 1 (ROCK1) rather than with RLC. Consequently, MYBPH inhibited ROCK1 and negatively regulated actomyosin organization, which in turn reduced single cell motility and increased collective cell migration, resulting in decreased cancer invasion and metastasis. Finally, we also show that *MYBPH* is epigenetically inactivated by promoter DNA methylation in a fraction of *TTF-1*-positive lung adenocarcinomas, which appears to be in accordance with its deleterious functions in lung adenocarcinoma invasion and metastasis, as well as with the paradoxical association of *TTF-1* expression with favourable prognosis in lung adenocarcinoma patients.

The EMBO Journal (2012) **31**, 481–493. doi:10.1038/emboj.2011.416; Published online 15 November 2011
Subject Categories: cell & tissue architecture
Keywords: actomyosin; cytoskeleton; lung cancer; ROCK1

Introduction

Metastasis is thought to be initiated by disruption of cell–cell contact, followed by single cell migration. It is widely accepted that contractile motion of cancer cells is generated by assembly and consecutive contraction of actomyosin bundles (Lauffenburger and Horwitz, 1996; Friedl and Wolf, 2003; Hall, 2009). Collective cell migration has been shown to result from decreasing actomyosin contractility at the sites of cell–cell contact and plays a role in a range of developmental processes as well as cancer invasion (Christiansen and Rajasekaran, 2006; Hidalgo-Carcedo *et al*, 2011).

Non-muscle myosin II (NM II), a major component of the actomyosin cytoskeleton, comprising two non-muscle myosin heavy chains (NMHCs) and two essential myosin light chains (ELCs), as well as two regulatory light chains (RLCs) (Conti and Adelstein, 2008; Vicente-Manzanares *et al*, 2009). Emerging evidence indicates that NM II members, especially NM IIA, are crucially involved in cancer cell migration, invasion, and metastasis via bivalent binding to actin filaments (Betapudi *et al*, 2006; Huang *et al*, 2009; Medjkane *et al*, 2009). Rho kinase 1 (ROCK1), a downstream effecter of RhoA, is a major positive regulator of that process, which is thought to be executed through phosphorylation of RLC and subsequent unfolding of NM IIA into an assembly competent form capable of NM IIA dimer formation. In addition, ROCK1 phosphorylates LIM domain kinase (LIMK) and stabilizes actin filaments through inactivation of the actin-depolymerizing factor cofilin. Another member of the ROCK family, ROCK2, is abundantly and preferentially expressed in non-epithelial tissues such as the brain and muscles, and plays roles in phagocytosis and cell contraction (Etienne-Manneville and Hall, 2002; Riento and Ridley, 2003; Amano *et al*, 2010). However, how actomyosin organization in non-muscle cells is negatively regulated to counterbalance the positive regulatory function of ROCK1 largely remains to be elucidated.

TTF-1 is a lineage-specific transcription factor required for branching morphogenesis and physiological lung functions (Kimura *et al*, 1996). TTF-1 is also involved in pathological conditions of the lung. For example, TTF-1 expression is prominent in lung epithelial cells undergoing regeneration (White *et al*, 2001; Pogach *et al*, 2007). A major fraction of lung adenocarcinomas are also TTF-1 positive, which is suggested to reflect their derivation from the terminal respiratory unit (Yatabe *et al*, 2002; Takeuchi *et al*, 2006). We and others recently identified TTF-1 as a lineage-survival oncogene with focal amplification in lung adenocarcinomas (Kendall *et al*, 2007; Tanaka *et al*, 2007; Weir *et al*, 2007; Kwei *et al*, 2008). However, it is of note that *TTF-1* expression is associated with favourable prognosis in lung adenocarcinoma cases (Anagnostou *et al*, 2009). In the present study, we identified MYBPH as a transcriptional target of TTF-1, which provides a clue for elucidating the molecular mechanism related to how TTF-1 paradoxically inhibits cancer invasion and metastasis.

Results

MYBPH is directly transactivated by TTF-1

As an initial step towards a better understanding of transcriptomes regulated by *TTF-1*, microarray analysis was

*Corresponding author. Division of Molecular Carcinogenesis, Center for Neurological Diseases and Cancer, Nagoya University Graduate School of Medicine, 65 Tsurumai, Showa-ku, Nagoya 466-8550, Japan. Tel.: +81 52 744 2454; Fax: +81 52 744 2457; E-mail: tak@med.nagoya-u.ac.jp

Received: 28 May 2011; accepted: 18 October 2011; published online: 15 November 2011

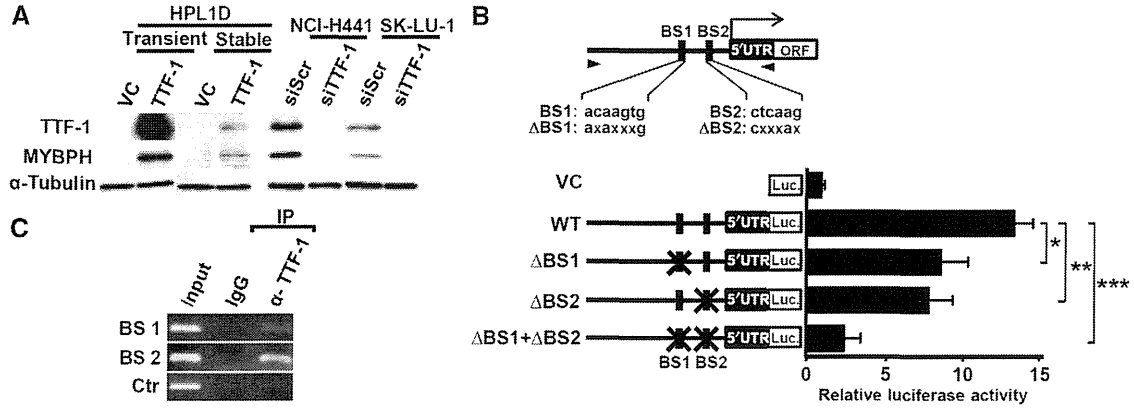

Figure 1 *MYBPH* is directly transactivated by TTF-1. (**A**) Western blot analysis showing induction of MYBPH in HPL1D cells transiently or stably transfected with TTF-1, as well as reduction by TTF-1 knockdown in NCI-H441 and SK-LU-1 cells. siScr, negative control siRNA; siTTF-1, siRNA against TTF-1. (**B**) Top panel: schematic diagram of *MYBPH* promoter region, BS1 and BS2, putative NKX2-5 and TTF-1 binding sites, respectively. Arrowheads, locations of primers used to amplify *MYBPH* promoter. Bottom panel: luciferase reporter analysis using HPL1D cells with transient TTF-1-expression. Three independent experiments were performed in triplicate. Bars, mean ± s.d.; $^{*}P<0.05$; $^{**}P<0.01$; $^{***}P<0.005$. (**C**) Chromatin immunoprecipitation assay of NCI-H441 cells showing that TTF-1 protein binds to both BS1 and BS2. Figure source data can be found with the Supplementary data.

performed using an immortalized peripheral lung epithelial cell line, HPL1D (Masuda *et al*, 1997), which was transiently transfected with *TTF-1*. We consequently identified *MYBPH* as the most highly upregulated gene (Supplementary Figure S1) and confirmed its upregulation at the protein level by western blot analysis (Figure 1A). A dual-luciferase assay also revealed *TTF-1*-mediated transcriptional activation of *MYBPH* (Figure 1B; Supplementary Figure S2A), while a chromatin immunoprecipitation (ChIP) assay of NCI-H441 cells clearly demonstrated specific binding of TTF-1 with both potential TTF-1 binding sites in the *MYBPH* promoter (Figure 1C).

MYBPH expression is inactivated by the promoter CpG methylation

TTF-1 was invariably present in lung adenocarcinoma cell lines expressing MYBPH at readily detectable levels (Figure 2A), while a significant correlation between TTF-1 and MYBPH expression was also observed in the analysis of our previous microarray data set of 90 lung adenocarcinoma cases ($P=0.0051$; Figure 2B; Takeuchi *et al*, 2006). Interestingly, however, we noted that a considerable fraction of lung adenocarcinomas both *in vitro* and *in vivo* expressed low levels of *MYBPH* despite high *TTF-1* expression. Therefore, we evaluated whether aberrant DNA methylation of the *MYBPH* promoter was involved in silencing of *MYBPH*. Treatment with a DNA demethylating agent, 5-Aza-dC, significantly induced *MYBPH* in NCI-H358 and A427 cells (Figure 2C), while bisulphite sequencing analysis revealed clear distinctions in terms of dense DNA methylation surrounding the genuine TTF-1 binding site (BS2; Li *et al*, 1998), but not that for the TTF-1 homologue, NKX2-5 (BS1; Chen and Schwartz, 1995), in NCI-H358 and A427 cells (Figure 2D; Supplementary Figure S2B). Methylation-specific PCR (MSP) analysis using DNA from laser microdissected specimens further confirmed the presence of aberrant DNA methylation specifically in *MYBPH*$^{-}$/*TTF-1*$^{+}$ lung adenocarcinoma tissues *in vivo* (Figure 2E). The present findings thus indicate that *MYBPH* is a direct transcriptional target of *TTF-1*, which is inactivated by promoter DNA methylation in a considerable fraction of lung adenocarcinomas.

MYBPH reduces cell motility, invasion, and metastasis

NM II is a major component of the actomyosin cytoskeleton in non-muscle cells and crucially involved in cell migration (Betapudi *et al*, 2006; Conti and Adelstein, 2008; Huang *et al*, 2009; Medjkane *et al*, 2009; Vicente-Manzanares *et al*, 2009). The presence of inactivating promoter DNA methylation led us to speculate that *TTF-1*-induced *MYBPH* might play a negative regulatory role in cell motility. Indeed, we found that treatment with small interfering RNA (siRNA) against *MYBPH* (siMYBPH) markedly increased the motility of NCI-H441 cells. Conversely, overexpression of MYBPH reduced Madin-Darby canine kidney (MDCK) cell motility (Figure 3A; Supplementary Figure S3), while that negative effect was cancelled by simultaneous treatment with siMYBPH (Supplementary Figure S4). Similarly, acquisition of the motile phenotype in siMYBPH-treated NCI-H441 cells was clearly demonstrated by results of a scratch assay (Figure 3B) as well as those of a Matrigel invasion assay (Figure 3C), with opposite effects observed in MYBPH-overexpressing MDCK cells. Next, we employed a three-dimensional Matrigel invasion assay and found that MYBPH-overexpressing MDCK cells invaded over a shorter distance and in a more collective manner than the control cells (Figure 3D). Neither siMYBPH treatment of NCI-H441 cells nor forced MYBPH overexpression in MDCK cells had an effect on cell growth (Supplementary Figure S5). We also noted that overexpression of TTF-1 reduced cell motility in HPL1D cells, which was significantly reverted by siMYBPH treatment (Figure 3E), supporting the notion that TTF-1-induced MYBPH negatively affects cell motility.

We also evaluated the effects of MYBPH expression on metastasis using a highly metastatic MYBPH-negative lung cancer cell line, NCI-H460-LNM35 (Kozaki *et al*, 2000). Stable transfectants expressing MYBPH at a level comparable to that in lung adenocarcinoma cell lines (Figure 4A) exhibited significantly reduced lung metastasis (Figure 4B and C), without affecting primary tumour growth (Supplementary Figure S6). Conversely, siMYBPH-treated NCI-H441 cells exhibited increased experimental lung metastasis (Figure 4D and E). In line with the present experimental findings, it was noted that decreased *MYBPH* expression was significantly

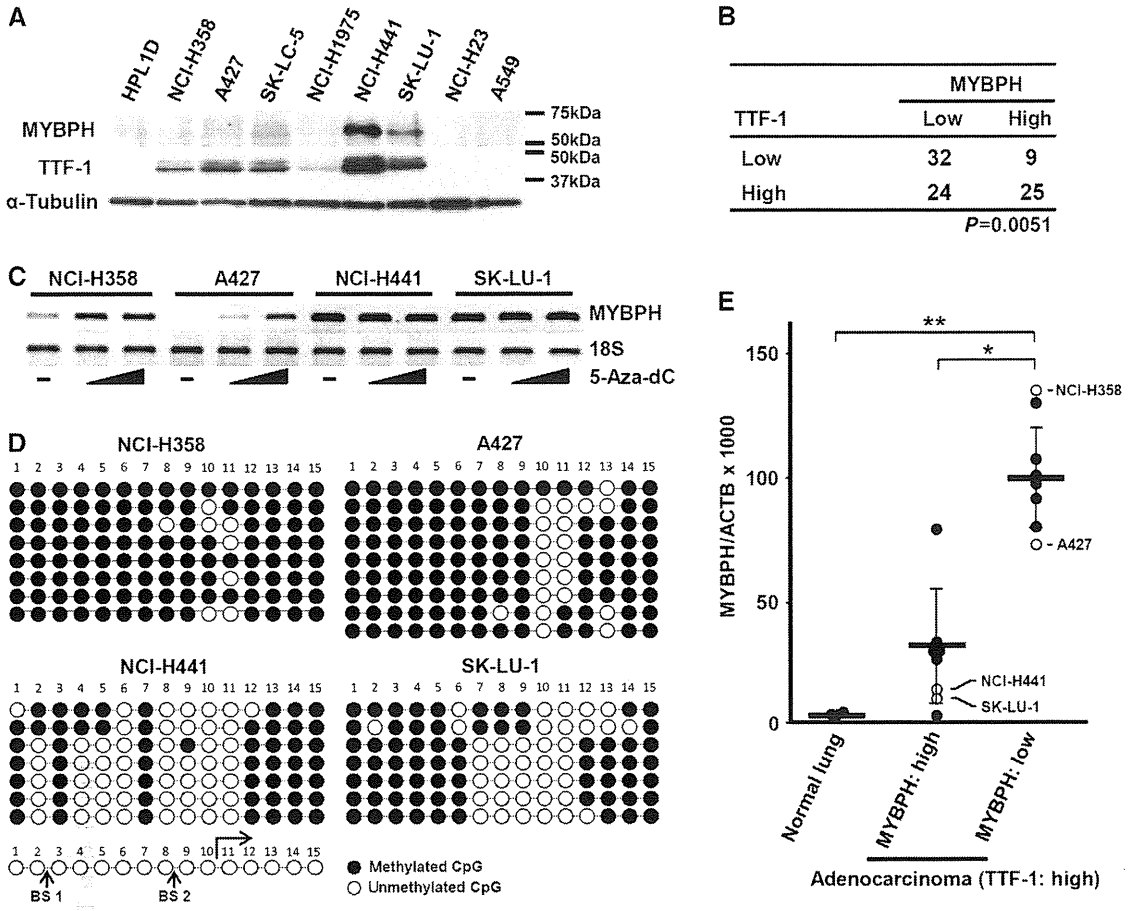

Figure 2 MYBPH expression is inactivated by the promoter CpG methylation. (**A**) Western blot analysis of MYBPH and TTF-1 in lung adenocarcinoma cell lines. (**B**) Correlation between *TTF-1* and *MYBPH* expressions in 90 lung adenocarcinoma specimens. Cases were classified into those above or below the average level of expression. (**C**) Semiquantitative RT–PCR analysis of four cell lines showing *MYBPH* induction in TTF-1-1$^+$/MYBPH$^-$-NCI-H358 and A427 cells after treatment with 5-Aza-dC. 18S served as a loading control. (**D**) Bisulphite sequencing analysis showing dense DNA methylation around BS2 in TTF-1$^+$/MYBPH$^-$-NCI-H358 and A427 cells. (**E**) Methylation-specific PCR analysis of the eighth CpG site in (**D**) using DNA from laser microdissected specimens and representative cell lines, which revealed aberrant DNA methylation in TTF-1$^+$/MYBPH$^-$ lung adenocarcinoma tissues and cell lines. Six cases each of MYBPH-positive and -negative lung adenocarcinomas with abundant TTF-1 expression, along with three normal lung tissues were analysed. Solid circles, clinical samples; open circles, cell lines; bars, mean ± s.d.; $^*P<0.001$; $^{**}P<0.0001$. Figure source data can be found with the Supplementary data.

associated with more apparent invasiveness in surgical specimens obtained from the 90 human lung adenocarcinoma cases (Figure 4F).

MYBPH affects actomyosin organization and cell morphology

We also found that siMYBPH treatment markedly altered the shape of the cells, as they showed a rounded morphology or occasionally bleb-like structures characterized by the appearance of peripheral actomyosin bundles, with clear colocalization of NMHC IIA with the peripheral actin bundles (Figure 5A; Supplementary Figure S7, left). Conversely, overexpression of MYBPH disrupted actomyosin organization as well as the normal morphology in MDCK cells (Figure 5B; Supplementary Figure S7, right). Taken together, these findings strongly support the notion that MYBPH is involved in the regulation of cell shape, motility, invasion, and metastasis.

MYBPH inhibits phosphorylation of RLC through interaction with ROCK1

Our findings strongly suggested that MYBPH is involved in actin organization. We, therefore, analysed changes in the proportion of triton-insoluble F-actin (TIF), a crosslinked meshwork of actin filaments that includes stress fibers (Watts and Howard, 1992), in relation to the level of MYBPH expression. We observed that siMYBPH-treated NCI-H441 cells contained a larger proportion of TIF pools than those treated with the siRNA control. In contrast, *MYBPH*-introduced MDCK cells contained fewer TIF pools than the control cells (Figure 6A).

Phosphorylation of RLC unfolds assembly incompetent NM IIA into assembly competent NM IIA, which is a prerequisite for its assembly and subsequent actomyosin reorganization (Conti and Adelstein, 2008; Vicente-Manzanares *et al*, 2009). In this connection, we found that NCI-H441 knocked down for *MYBPH* exhibited increased RLC phosphorylation, whereas introduction of *MYBPH* reduced the RLC phosphorylation level in MDCK cells (Figure 6B). This finding prompted us to investigate whether MYBPH is involved in the regulation of ROCK-mediated phosphorylation of RLC, since ROCK1 and 2 have been shown to play a central role in the regulation of RLC phosphorylation as downstream effectors of RhoA (Conti and Adelstein, 2008; Vicente-Manzanares *et al*, 2009). *In-vitro* protein–protein binding

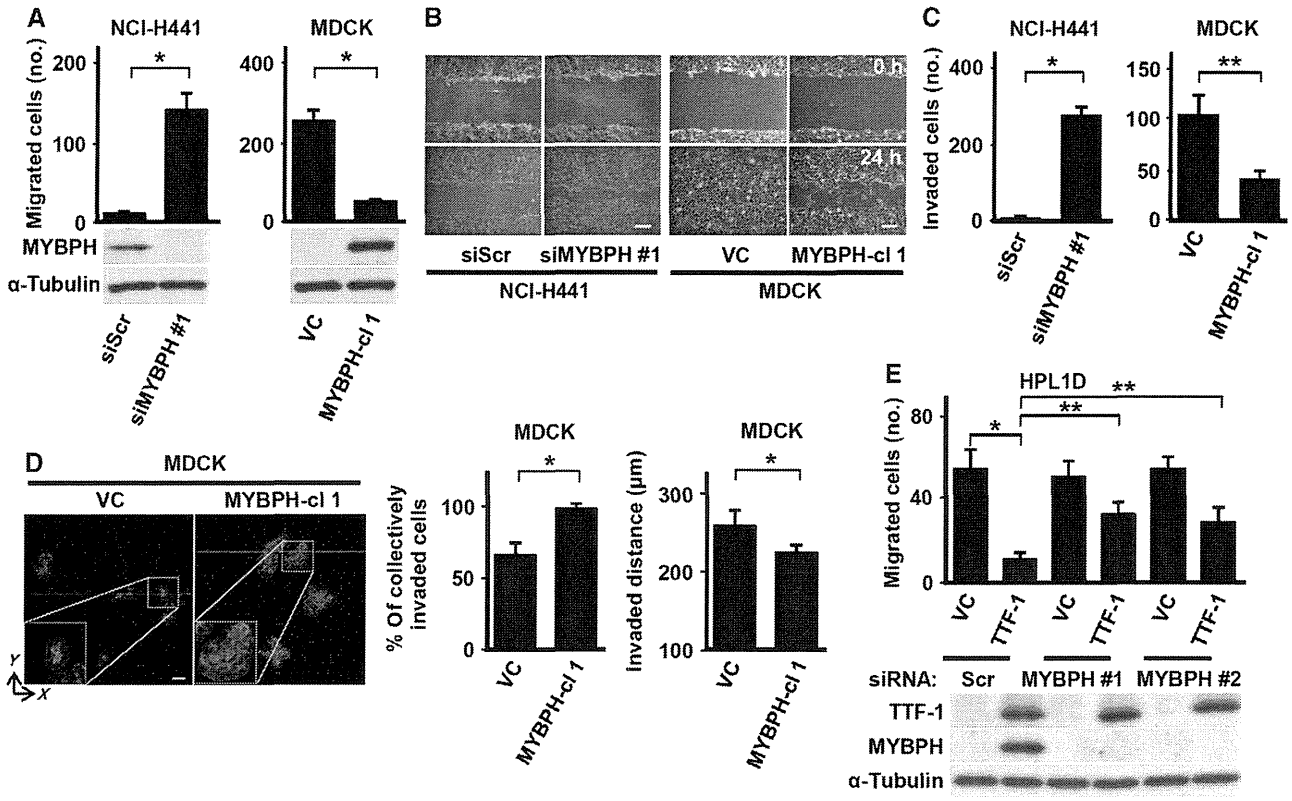

Figure 3 MYBPH reduces cell motility and invasion *in vitro*, and increases collective cell migration. (**A**) Motility assay showing increased *in-vitro* motility by MYBPH knockdown in NCI-H441 cells as well as reduced motility in stable MYBPH transfectant of MDCK cells. Three independent experiments were performed in triplicate. siMYBPH, siRNA against MYBPH; MYBPH-cl 1, MYBPH-transfected clone; bars, mean ± s.d.; $^{*}P<0.01$. Results of corresponding western blot analysis of MYBPH are shown below. (**B**) Scratch assay showing increased *in-vitro* motility by MYBPH knockdown in NCI-H441 cells as well as reduced motility in stable MYBPH transfectant of MDCK cells. Photographs were taken at 24 h after scratch injury. Bars indicate 200 μm. (**C**) Matrigel invasion assay showing increased *in-vitro* invasion by MYBPH knockdown in NCI-H441 cells as well as reduced invasion in stable MYBPH transfectant of MDCK cells. Three independent experiments were performed in triplicate. Bars, mean ± s.d.; $^{*}P<0.001$; $^{**}P<0.01$. (**D**) Three-dimensional Matrigel invasion assay showing collective cell migration and decreased *in-vitro* invasion in stable MYBPH transfectant of MDCK cells. The proportions of cells with collective invasion were evaluated as described in Materials and methods. Data shown represent four independent experiments each counting > 100 cells. White bars indicate 50 μm. Bars, mean ± s.d.; $^{*}P<0.001$. (**E**) Motility assay findings showing reduced *in-vitro* motility in stable TTF-1 transfectants of HPL1D cells, which was cancelled by treatment with siMYBPH. Three independent experiments were performed in triplicate. Bars, mean ± s.d.; $^{*}P<0.01$; $^{**}P<0.05$. The results of corresponding western blot analyses of TTF-1 and MYBPH are shown below. Figure source data can be found with the Supplementary data.

assays were performed to examine whether MYBPH directly interacts with RLC and/or ROCK1 and 2, using a purified His-tagged MYBPH protein with either purified GST-tagged ROCK1, ROCK2, or RLC proteins. Consequently, a direct interaction of MYBPH specifically with ROCK1, but not with RLC, was unexpectedly revealed (Figure 6C). *In-vitro* ROCK kinase assays using purified ROCK1, ROCK2, and RLC proteins in the presence or absence of purified MYBPH protein demonstrated inhibition of ROCK1-mediated RLC phosphorylation by inclusion of MYBPH in the reaction mixture, whereas the presence of MYBPH had no effects on ROCK2-mediated RLC phosphorylation *in vitro*, consistent with the *in-vitro* binding assay results (Figure 6D; Supplementary Figure S8). We also noted that MYBPH was not phosphorylated by either ROCK1 or ROCK2 (Supplementary Figure S8). Immunoprecipitation–western blot (IP–WB) analysis also showed an association of MYBPH with ROCK1 in MYBPH-overexpressing MDCK and NCI-H441 cells, respectively (Figure 6E; Supplementary Figure S9). Overexpression of MYBPH reduced the interaction between ROCK1 and RLC in MDCK, whereas siMYBPH treatment increased their interaction in NCI-H441 cells (Figure 6F). In contrast, the interaction between RhoA and ROCK1 was not affected by MYBPH (Supplementary Figure S10), which appears to be consistent with the interaction of MYBPH with purified GST-tagged ROCK1 protein lacking a RhoA-binding domain near the C-terminus. In addition, IP–WB analysis showed lack of interactions of MYBPH with various RLC kinases (Supplementary Figure S11), including myosin light chain kinase (MLCK), myotonic dystrophy kinase-related CDC42 binding protein kinase alpha and beta (MRCKα and β), citron, and Zipper interacting protein kinase (ZIPK) (Matsumura, 2005).

Further analysis using various deletion mutants of MYBPH showed that the fibronectin type III domain of MYBPH was required for MYBPH binding to ROCK1 (Figure 7A; Supplementary Figure S12). Consistently, a deletion mutant devoid of the fibronectin type III domain did not elicit MYBPH overexpression-induced alterations in cell morphology and actomyosin bundle formation or decreased cell motility in MDCK cells (Figure 7B; Supplementary Figure S13). We also found that MYBPH affects the phosphorylation state of LIMK and cofilin (Figure 7C), which are known to participate in the cascade downstream of ROCK1, thus regulating actin polymerization (Maekawa *et al*, 1999; Yoshioka

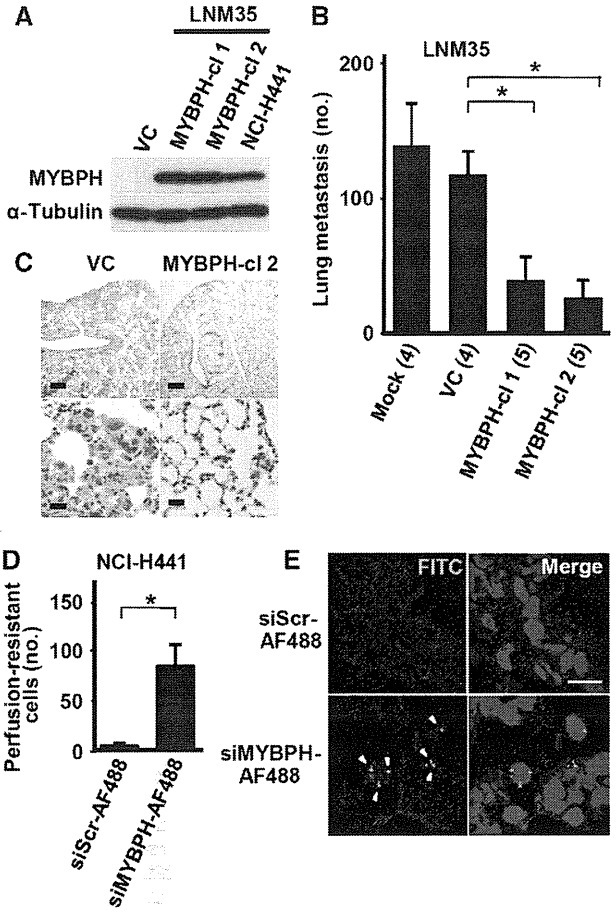

F

Invasion	MYBPH Low	MYBPH High
Definite	46	19
Definite but focal	8	7
Negligible/Negative	2	8

P=0.0065

Figure 4 MYBPH reduces invasion and metastasis *in vivo*. (**A**) Western blot analysis showing expression levels of MYBPH in stable transfectants of NCI-H460-LNM35 (LNM35-MYBPH-cl 1 and -cl 2) expressing MYBPH at a level comparable to that in NCI-H441. (**B**) Decreased lung metastasis in stable MYBPH transfectants of LNM35. Forty days after subcutaneous inoculation, lung metastases were counted. Bars, mean ± s.d.; $^*P<0.01$. Numbers in parentheses indicate inoculated mice. (**C**) Representative haematoxylin and eosin-stained images of lung metastases. Bars indicate 200 μm in upper and 20 μm in lower panels. (**D**) Experimental metastasis assay of NCI-H441 cells knocked down for MYBPH with Alexa Fluor 488-conjugated siMYBPH #1 (siMYBPH #1-AF488) (five mice per treatment). Bars, mean ± s.d.; $^*P<0.001$. (**E**) Representative fluorescence images of perfusion-resistant cells. Cells were also stained with DAPI (blue). Bars indicate 10 μm. (**F**) Relationships between *MYBPH* expression and invasion status in our previously reported microarray data set of human lung adenocarcinomas. Cases were classified into those above and below the average level of expression. Figure source data can be found with the Supplementary data.

et al, 2003). Consistent with the present findings, increased motility, RLC phosphorylation, and organization of peripheral actomyosin bundles induced by MYBPH knockdown in NCI-H441 cells were significantly, though not completely, counteracted by simultaneous treatment with the ROCK-specific inhibitor Y-27632 (Figure 7D; Supplementary Figure S14). It was also found that increased cell motility and RLC phosphorylation induced by siMYBPH treatment were counteracted by simultaneous treatment with siROCK1, but not with siROCK2 (Figure 7E). Thus, it was demonstrated that MYBPH binds to ROCK1 but not to RLC, leading to inhibition of ROCK1-mediated regulation of actomyosin organization including assembly competence-conferring RLC phosphorylation and activation of the LIMK–cofilin pathway.

MYBPH increases cell–cell contact and collective cell migration

A decrease in ROCK-driven actomyosin contractility enhances cell–cell contact and collective cancer cell invasion (Sahai and Marshall, 2002; Hidalgo-Carcedo *et al*, 2011). Along this line, NCI-H441 cells knocked down for MYBPH migrated mostly as single cells in a three-dimensional invasion assay, which was reverted by simultaneous treatment with Y-27632 (Figure 8A). This siMYBPH-mediated increase in single cell migration was markedly counteracted by simultaneous treatment with siROCK1 (Figure 8B). While one of the hallmarks characterizing collective cell migration is preservation of the integrity of cell–cell contact during movement (Friedl and Gilmour, 2009), MYBPH knockdown markedly decreased cell–cell contact in NCI-H441 cells, as shown in our aggregation assay. This effect was clearly counteracted by a simultaneous treatment with Y-27632 (Figure 8C). Conversely, overexpression of MYBPH reduced MDCK cell aggregation (Figure 8D). Formation of adherence junctions positively regulate cell–cell contacts in epithelial cells (Friedl and Wolf, 2010). Our aggregation assay findings showed that siMYBPH-treated NCI-H441 cells exhibited a readily detectable decrease in E-cadherin staining intensity on the cell surface, which was considerably counteracted by simultaneous treatment with Y-27632 (Figure 8E). Conversely, overexpression of MYBPH increased E-cadherin intensity in MDCK cells similarly examined by an aggregation assay (Supplementary Figure S15). Interestingly, western blot analysis demonstrated similar levels of E-cadherin expression irrespective of MYBPH state. Taken together, the present findings indicate that TTF-1-inducible MYBPH inhibits ROCK1 through direct interaction, which in turn negatively regulates actomyosin organization, leading to decreased cell motility, invasion, and metastasis (Figure 9).

Discussion

The present findings indicate that *MYBPH*, which we identified here as a direct transcriptional target of *TTF-1*, plays multiple roles in negative regulation of actomyosin organization. Among the various myosin binding proteins, a cardiac isoform of *MYBPC* (*cMYBPC*) has been the focus of intense research activities, because of its direct involvement in cardiovascular diseases such as familial hypertrophic cardiomyopathy (Bonne *et al*, 1995; Watkins *et al*, 1995; Richard *et al*, 2003). While *MYBPH* and *cMYBPC* possess significant homology at their carboxyl termini, *MYBPH* lacks a region homologous to the amino terminal half of *cMYBPC*, which is required for inhibition of myosin functions. To date, very little is known about the functions of *MYBPH*, even in regard to its interaction with muscle myosin (Yamamoto, 1988; Welikson and Fischman, 2002), with virtually nothing reported regarding its roles in non-muscle cells.

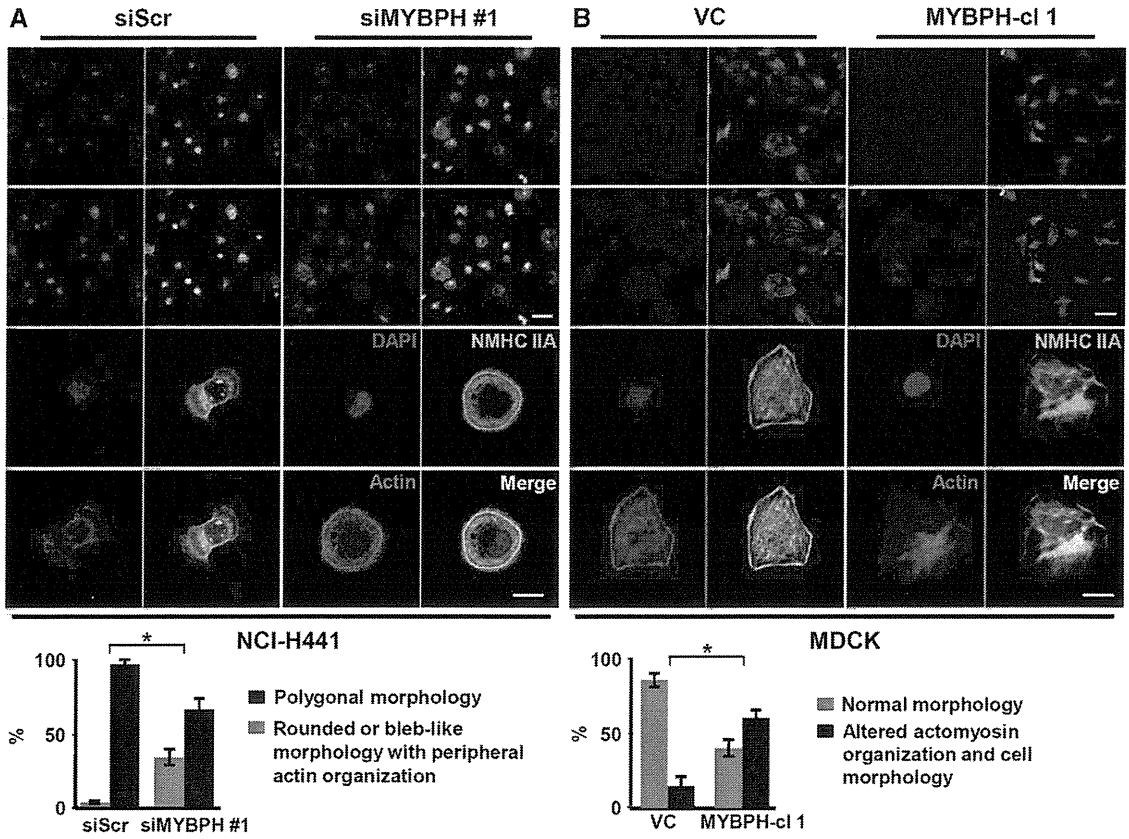

Figure 5 MYBPH affects actomyosin organization and cell morphology. (**A**) Top panels: immunofluorescence staining for DAPI (blue), actin (red), and NMHC IIA (green) in NCI-H441 cells treated with siScr or siMYBPH. Bars indicate 100 μm in top and 10 μm in bottom panels. Bottom panel: proportions of cells according to morphology. Data shown represent three independent experiments each counting >100 cells. Bars, mean ± s.d.; $^*P<0.001$. Results with an additional siMYBPH are also shown in the left panels of Supplementary Figure S7. (**B**) Top panels: immunofluorescence staining for DAPI (blue), actin (red), and NMHC IIA (green) in MDCK cells stably transfected with empty or MYBPH-expressing vectors. Bars indicate 100 μm in top and 10 μm in bottom panels. Bottom panel: proportions of cells according to morphology, which were determined as shown in (**A**). Bars, mean ± s.d.; $^*P<0.001$. Results obtained with an additional independent clone are shown in the right panels of Supplementary Figure S7.

In this study, we found that MYBPH inhibits assembly competence-conferring RLC phosphorylation as well as activating phosphorylation of LIMK. MYBPH unexpectedly executes such inhibitory activities by direct physical interaction with ROCK1 rather than with RLC, which results in inhibition of ROCK1 kinase activity. ROCK1 is a downstream effector of RhoA that is crucially involved in cell morphogenesis and motility, as well as in cancer progression (Itoh *et al*, 1999; Sahai and Marshall, 2003; Wilkinson *et al*, 2005; Wong *et al*, 2008). To date, however, very few examples have been reported as negative regulators of ROCK1. While RhoE has been shown to inhibit ROCK1 by competing with RhoA for ROCK1 (Riento *et al*, 2003), MYBPH directly binds to and interferes with ROCK1, which in turn inhibits RLC phosphorylation. Our findings thus add MYBPH to the small list of negative ROCK1 regulators, suggesting a complex nature of the negative regulatory mechanisms of ROCK1.

It is interesting that marked distinctions were observed in terms of specificities of the binding and inhibitory capabilities of MYBPH towards ROCK1 and ROCK2. Along line, it is important to note that RhoE binds to ROCK1 but not to ROCK2 and inhibits its function, resulting in loss of stress fiber formation (Riento *et al*, 2003). It was also reported that siRNA-mediated ROCK1 knockdown results in loss of stress fibers, in contrast to lack of such effects in cells knocked down for ROCK2 (Yoneda *et al*, 2005). Together, these findings indicate that ROCK1 plays a major role in stress fiber formation and are in line with the present findings of actomyosin regulation by MYBPH through ROCK1 inhibition.

Considering that ROCK1 also mediates regulatory phosphorylation of various other molecules, such as endothelial nitric oxide synthase (eNOS) and collapsin response mediator protein 2 (CRMP2), and is involved in a wide range of disease states including vasospasms, pulmonary hypertension, and nerve injury (Etienne-Manneville and Hall, 2002; Riento and Ridley, 2003), it would be interesting to investigate whether MYBPH might be involved in such disease states as a regulator of ROCK1. In addition, given that collective cell migration plays an important role in various physiological settings including morphogenesis, tissue regeneration, and repair of wounded epithelial tissues (Kimura *et al*, 1996; White *et al*, 2001; Pogach *et al*, 2007), it is of note that changes in MYBPH expression alter actomyosin organization, and consequently affect collective cell migration, especially when considering that TTF-1 is a master regulatory transcription factor involved in peripheral lung development (Kimura *et al*, 1996; Yatabe *et al*, 2002) and that type II pneumocyte hyperplasia, a reconstitution process of the alveolar lining, is associated with increased TTF-1expression (White *et al*, 2001; Pogach *et al*, 2007).

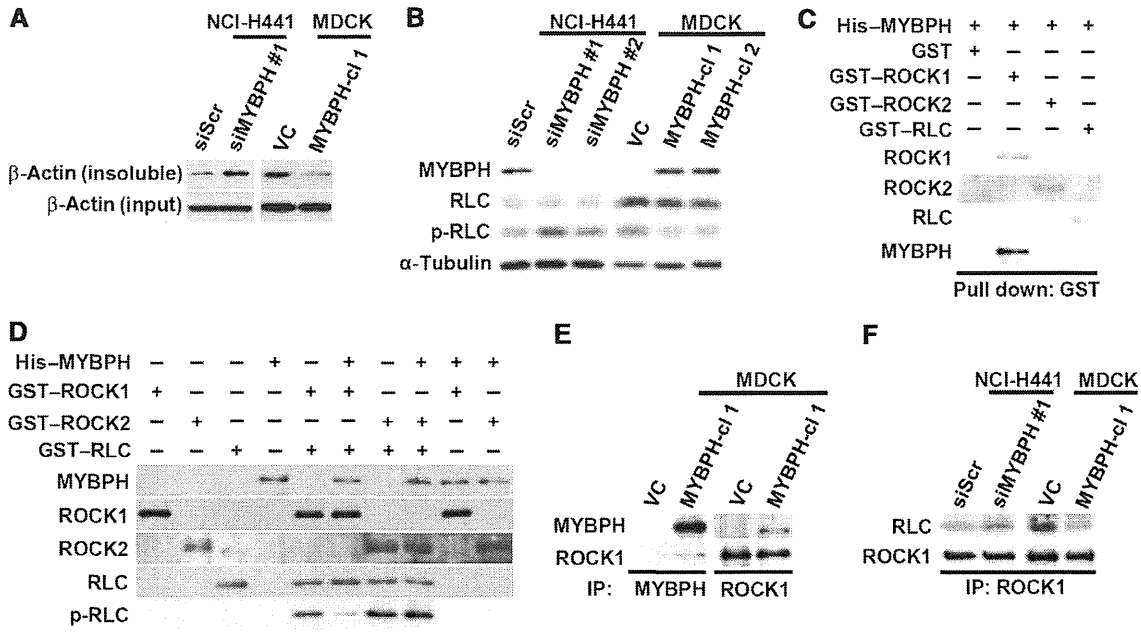

Figure 6 MYBPH inhibits phosphorylation of RLC through interaction with ROCK 1. (**A**) Actin assembly assay showing an increase in triton-insoluble unassembled F-actin (TIF) in siMYBPH-treated NCI-H441 cells as well as opposite effects by MYBPH introduction in MDCK cells. (**B**) Western blot analysis showing induction of RLC phosphorylation by MYBPH knockdown in NCI-H441 cells as well as reduction in MYBPH transfectants of MDCK cells. p-RLC, phospho-RLC (T18/S19). (**C**) *In-vitro* protein–protein binding assay results showing interaction of purified MYBPH with ROCK1, but not with ROCK2 or RLC. (**D**) *In-vitro* ROCK kinase assay using purified RLC protein as a substrate, showing inhibition of ROCK1-mediated RLC phosphorylation by MYBPH. (**E**) Immunoprecipitation–western blot (IP–WB) analysis showing co-immunoprecipitation of MYBPH with ROCK1 in MDCK cells expressing exogenous MYBPH. (**F**) IP–WB analysis showing increased interaction between ROCK1 and RLC by siMYBPH treatment in NCI-H441 cells. Conversely, their reduced interaction was seen in MDCK cells stably transfected with MYBPH. Figure source data can be found with the Supplementary data.

Our results clearly demonstrate that MYBPH negatively regulates cell motility, invasion, and metastasis. Thus, it is quite conceivable that *MYBPH* induction by *TTF-1* is deleterious for lung adenocarcinoma progression, which is thereby inactivated by promoter DNA methylation in a fraction of *TTF-1*-positive lung adenocarcinomas. This finding in turn resolves a question arising from previous observations that a high level of *TTF-1* expression, which we and others have identified as a lineage-survival oncogene in lung adenocarcinoma (Kendall *et al*, 2007; Tanaka *et al*, 2007; Weir *et al*, 2007; Kwei *et al*, 2008), is paradoxically associated with favourable prognosis (Anagnostou *et al*, 2009). We note that during the preparation of this manuscript, Jacks and colleagues reported that TTF-1 downregulation was associated with tumour progression and acquisition of metastatic ability, in association with derepression of HMGA2 in a lung adenocarcinoma model of mutant K-ras/p53 conditional knockout (Winslow *et al*, 2011). Our findings further indicate that MYBPH plays a crucial role as a positively regulated downstream effector of TTF-1, with capabilities for inhibiting cancer cell motility, invasion, and metastasis. Thus, both transcriptional activation and repression by TTF-1 appear to be engaged in conferring a less aggressive phenotype, despite its opposing role as a lineage-survival oncogene in TTF-1-positive lung adenocarcinomas (Kendall *et al*, 2007; Tanaka *et al*, 2007; Weir *et al*, 2007; Kwei *et al*, 2008).

Materials and methods

Cell lines

The derivation, characteristics, and culture conditions of the human lung adenocarcinoma cell lines utilized, and the immortalized human lung epithelial cell line HPL1D as well as the highly metastatic NCI-H460-LNM35 (LNM35) lung cancer cell line were previously reported (Masuda *et al*, 1997; Kozaki *et al*, 2000; Tanaka *et al*, 2007). An MDCK cell line was purchased from RIKEN Cell Bank and maintained in Dulbecco's Modified Eagle's Medium containing 10% fetal bovine serum.

Antibodies, reagents, and oligonucleotide primers

The anti-TTF-1 antibody for western blot analysis was purchased from DAKO; anti-TTF-1 for the ChIP assay from Thermo; anti-MYBPH from Abnova; anti-E-cadherin from BD Transduction Laboratories; anti-GST and anti-His from MBL; anti-NMHC IIA, anti-MLCK, anti-β-actin, and anti-α-tubulin from Sigma-Aldrich; anti-ROCK1, anti-ROCK2, anti-RLC, anti-phospho-RLC (T18/S19), anti-cofilin, anti-phospho-cofilin (S3), anti-phospho-LIMK1 (T508)/LIMK2 (T505), anti-mouse IgG, and anti-rabbit IgG from Cell Signalling Technology; anti-Citron from Novus; anti-RhoA, anti-MRCK-α, and anti-MRCK-β from Santa Cruz; and anti-ZIPK from Calbiochem. ROCK-specific inhibitor Y-27632 was also purchased from Calbiochem. The sequences of the oligonucleotide primers used for PCR and sequencing are provided in Supplementary Table S1.

DNA constructs

The expression construct of full-length human *TTF-1* (pCMV puro-TTF-1) was previously described (Tanaka *et al*, 2007). Full-length human *MYBPH* cDNA (OpenBio) was inserted into a pCMV-puro vector and the entire open reading frame of the resultant construct (pCMVpuro-MYBPH) was thoroughly sequenced. Transfection was performed using FuGENE6 (Roche), followed by puromycin selection.

Microarray data

RNA was extracted from HPL1D cells transiently transfected with TTF-1 or an empty vector followed by puromycin selection for 3 days, and analysed in duplicate (GSE26721), using a low RNA fluorescent linear amplification kit and 44K whole human genome microarrays (Agilent Technologies), essentially as described previously (Tomida *et al*, 2009). Our previously obtained micro-

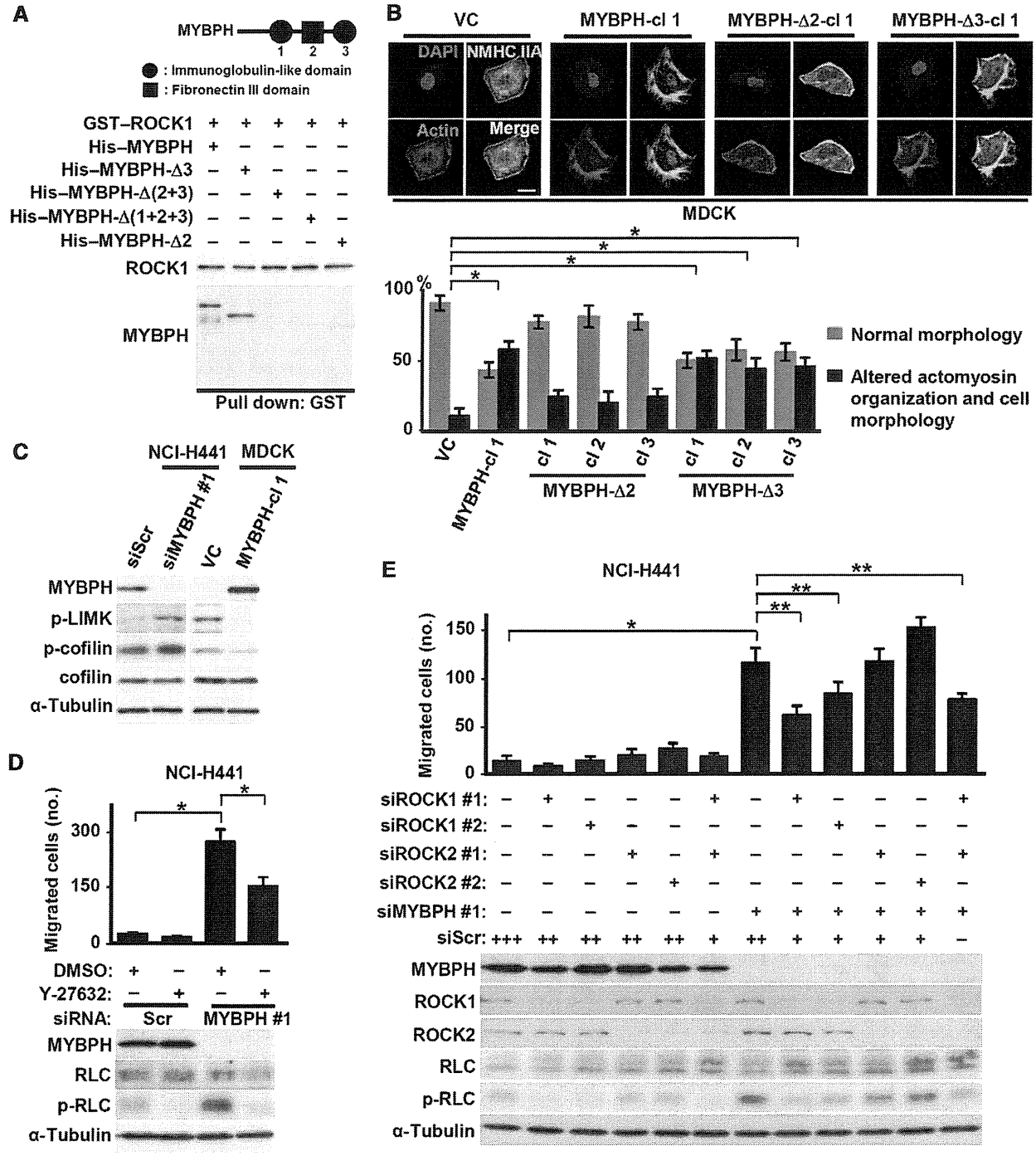

Figure 7 MYBPH knockdown-induced effects on actin bundle formation, cell motility and RLC phosphorylation are alleviated through ROCK1 binding and inhibition. (**A**) Top panel: schematic representation of domain organization of MYBPH. Bottom panel: *in-vitro* protein–protein binding assay showing requirement of a fibronectin type III domain of MYBPH for its binding with ROCK1. Western blot analysis of His-tagged MYBPH-wt, -Δ3, -Δ(2 + 3), -Δ(1 + 2 + 3), and -Δ2 proteins are shown in Supplementary Figure S12. (**B**) Top panels: immunofluorescence staining for DAPI (blue), actin (red), and NMHC IIA (green) in MDCK cells stably introduced with an empty vector (VC), or MYBPH expression constructs of wild-type or deletion mutants lacking either fibronectin type III (MYBPH-Δ2) or immunoglobulin-like domains. Bars indicate 10 μm. Bottom panel: proportions of cells according to morphology, which were determined as shown in Figure 5A. Bars, mean ± s.d.; $^{*}P<0.001$. (**C**) Western blot analysis showing induction of LIMK and cofilin phosphorylation by MYBPH knockdown in NCI-H441 cells as well as reduction in MYBPH transfectant of MDCK cells. p-LIMK, phospho-LIMK1 (T508)/LIMK2 (T505); p-cofilin, phospho-cofilin (S3). (**D**) Top panel: partial cancellation of the MYBPH knockdown-induced motility by a simultaneous treatment with a ROCK-specific inhibitor Y-27632 in NCI-H441 cells. Bars, mean ± s.d.; $^{*}P<0.01$. Bottom panel: representative western blot images for RLC phosphorylation. (**E**) Top panel: partial cancellation of MYBPH knockdown-induced motility by simultaneous treatment with siRNAs against ROCK1 in NCI-H441 cells. Bars, mean ± s.d.; $^{*}P<0.01$; $^{**}P<0.05$. Bottom panel: representative western blot images for RLC phosphorylation. siRNA concentrations: +, 40 nM; + +, 80 nM; + + +, 120 nM. Figure source data can be found with the Supplementary data.

array data of 90 lung adenocarcinoma cases (Takeuchi *et al*, 2006; GSE11969) were used to analyse the association of *MYBPH* expression with *TTF-1* expression as well as with various clinical parameters.

siRNA treatment

siRNA duplexes targeting TTF-1 (siTTF-1) and MYBPH (siMYBPH #1 and #2 as well as siMYBPH-AF488, Alexa Fluor 488-conjugated siMYBPH #1) and a negative control (siScr) were obtained from

Sigma Genosys, while siRNA duplexes targeting ROCK1 (siROCK1 #1 and #2) and ROCK2 (#1 and #2) from Invitrogen. Transfection of each siRNA at 40 nM was performed using Lipofectamine RNAi-MAX (Invitrogen). Cells were harvested at 48 h after transfection for each assay. The sequences of the siRNAs are provided in Supplementary Table S1.

Western blot analysis

Western blot analysis was performed according to standard procedures using Immobilon-P filters (Millipore) and an Enhanced Chemiluminescence system (GE Healthcare). NCI-H441 cells were treated with Y-27632 (5 μM) for 15 min before.

IP–WB analysis

Cells (2×10^7) were lysed with modified RIPA buffer containing protease inhibitor cocktail Tablets (Roche) and incubated with each antibody overnight at 4°C, followed by addition of protein G Sepharose (GE Healthcare) and subsequent incubation for an additional 1 h. The immunoprecipitates were analysed by western blot analysis.

Dual-luciferase reporter assay

An MYBPH *luciferase* reporter construct was generated using a pGL4 basic reporter vector (Promega) and a PCR-amplified 1.0-kb genomic fragment from the MYBPH promoter region. Mutant vectors carrying deletions at the predicted binding sites for *TTF-1* and *NKX2-5* were constructed using a QuikChange site-directed mutagenesis kit (Stratagene). HPL1D cells (3.0×10^5) transiently expressing *TTF-1* were transfected with each pGL4 vector (1.8 μg) together with a pRLTK vector (0.2 μg), then the cell lysates were collected after 48 h. Luciferase reporter activities were determined using a Dual-Luciferase Reporter Assay System (Promega). Firefly luciferase activity was normalized with that of Renilla luciferase.

ChIP assay

NCI-H441 cells (1.0×10^8) were harvested after crosslinking with 1% formaldehyde. Chromatin was sheared by sonication to an average length of 500–600 bp, followed by immunoprecipitation with a TTF-1-specific antibody. After reversal of crosslinking, immunoprecipitated chromatin was subjected to PCR using primers for the predicted binding sites of *TTF-1* and *NKX2-5* as well as those for an unrelated genomic region as a negative control.

Treatment with 5-aza-2′-deoxycytidine

Cells ($1.0–1.5 \times 10^5$) were incubated with 1 or 2 μM of 5-aza-2′-deoxycytidine (5-Aza-dC; Sigma) for 5 days. Media were changed every 24 h. Semiquantitative PCR was performed using primers for amplification of the coding region of MYBPH.

Bisulphite sequencing analysis

Bisulphite conversion of genomic DNA was performed using MethylEasy Xceed™ (Human Genetic Signatures), according to the manufacturer's instructions. The MYBPH promoter region was amplified using nested primers and the resultant PCR products were cloned into pGEM-T easy vectors (Promega), followed by sequencing of randomly selected clones.

Laser microdissection and MSP

Cancer cells were microdissected from 20 μm thick frozen sections using a Leica LMD 7000 Laser Micro-dissection system (Leica Microsystems). Bisulphite-modified DNA was used as a template for SYBR Green (Applied Biosystems)-based real-time PCR, with primers designed for specific detection of methylated DNA at a CpG (#8) close to the TTF-1-binding consensus sequence of the *MYBPH* promoter and a promoter region without CpG sites of the reference gene, *ACTB*. The methylation level in the *MYBPH* promoter was determined as the ratio of methylation-specific PCR-amplified *MYBPH* gene to *ACTB* reference gene, and then multiplied by 1000 for easier tabulation.

In-vitro motility, invasion, scratch, and MTT assays

In-vitro motility and invasion assays were essentially performed as previously described (Kozaki *et al*, 2000). For each assay, 1×10^5 MDCK cells, 1.5×10^5 NCI-H441, and HPL1D cells were added to the upper chambers, then incubated for 24, 36 and 36 h, respectively. NCI-H441 cells were treated with Y-27632 (5 μM) for 15 min before incubation. For a scratch assay, 1.5×10^6 cells were plated in 6-well plates. After 24 h of incubation, a single linear wound was created with a 200-μl pipette tip. An MTT assay was performed with TetraColor One (Seikagaku) according to the manufacturer's instructions.

Three-dimensional Matrigel invasion assay and immunostaining

One hundred microlitres of Matrigel (BD Biosciences) was prepared on 18 × 18 mm coverslips in 6-well plates, on which 2×10^5 cells were plated and cultured for 48 h, followed by fixation with 3.7% formaldehyde for 30 min and post-fixing with 0.1% Triton X-100 for 30 min at room temperature (RT). Cells were incubated with blocking buffer (1% BSA in PBS) overnight at 4°C and were visualized by staining with Alexa-conjugated phalloidin (Molecular Probes). The coverslips were mounted onto slides using Fluoromount (Diagnostic BioSystems) and analysed using an A1 Rsi confocal microscope (Nikon). The invasion distance was defined as that between the slide glass (top of the Matrigel) and the centre of fluorescence intensity, and measured using MetaMorph (Molecular Devices) software. The extent of collective cell migration was defined as the ratio of collective cells ($\geqslant 5$ cells) to total cell number. Data shown represent three independent experiments, with >100 cells counted in each.

In-vivo metastasis assay

LNM35 cells (1.0×10^7) in 0.1 ml of serum-free RPMI-1640 medium were injected into subcutaneous tissues of the right groin of 6-week-old female SCID mice. Forty days after inoculation, the mice were euthanized, and their lungs and subcutaneous tumours resected, weighed, and fixed with 10% formaldehyde. Lung-metastatic nodules were examined under a dissecting microscope. An experimental metastasis assay following tail vein injection of tumour cells was performed, essentially as described by Shibue and Weinberg (2009). NCI-H441 cells were transfected with either Alexa Fluor 488-conjugated siScr (siScr-AF488) or -siMYBPH #1 (siMYBPH-AF488) as described above, then the transfectants were harvested 48 h later. Cells at 1.0×10^6 in 0.1 ml of PBS were injected into tail veins of 6-week-old female SCID mice. Five days after injection, the mice were euthanized, then 6 ml of PBS was injected into the right ventricle for perfusion of the lung microvasculature. The perfused lungs were embedded in OCT (Sakura), sectioned (thickness 10 μm) with a Leica CM3050 (Leica Microsystems), and fixed using Fluoromount. Perfusion-resistant cells were determined by direct counting in the sections using an A1 Rsi confocal microscope.

Immunostaining

Cells (0.5×10^5) were plated on 18 × 18 mm coverslips in 6-well plates and cultured for 12 h. NCI-H441 cells were treated with Y-27632 (5 μM) for 15 min before plated. The cells were fixed by incubating with 3.7% formaldehyde for 10 min at RT, followed by post-fixing with 0.1% Triton X-100 for 10 min at RT. Cells were incubated with blocking buffer overnight at 4°C, followed by another incubation with antibodies (diluted in blocking buffer) for 60 min at RT. After treatment with Alexa-conjugated secondary antibodies (Molecular Probes) for 60 min at RT, the coverslips were mounted onto slides using Fluoromount, and analysed using an A1 Rsi confocal microscope.

Actin assembly assay

Cells were lysed with buffer containing 1% Triton X-100, 10 mM EGTA, 40 mM NaCl, 10 mM imidazole, and a protease inhibitor cocktail (Roche) at 4°C. The lysates were centrifuged at 15 000 × *g* for 5 min at 4°C, then the pellets were washed, dissolved in 1 × SDS sample buffer, and subjected to western blot analysis with an anti-actin antibody. Three independent experiments were performed in triplicate, with similar results obtained.

Preparation of recombinant proteins

His-tagged MYBPH-wt, -Δ3, -Δ(2 + 3), -Δ(1 + 2 + 3), and -Δ2 proteins were expressed in Sf9 insect cells using a Gateway system (Invitrogen), according to the manufacturer's instructions. Recombinant His-tagged MYBPH-wt, -Δ3, -Δ(2 + 3), -Δ(1 + 2 + 3), and -Δ2 proteins were purified using imidazole-affinity chromatography. Recombinant GST-tagged ROCK1 (amino acids 17–535) and GST-tagged ROCK2 (amino acids 5–554) were purchased from Sigma. GST-tagged RLC and GST were from Abnova.

In-vitro protein–protein binding assay

Purified His-tagged MYBPH-wt, -Δ3, -Δ(2 + 3), -Δ(1 + 2 + 3), or -Δ2 was mixed with glutathione beads coated with recombinant GST, GST-tagged RLC, GST-tagged ROCK1, or GST-tagged ROCK2. After repeated washes with a solution containing 20 mM MOPS (pH 7.2), 1 mM dithiothreitol, 5 mM EGTA, 25 mM β-glycerophosphate, 1 mM Na_3VO_4, and 75 mM $MgCl_2$, the bound proteins were eluted and subjected to SDS–PAGE, followed by western blot analysis with anti-ROCK1, anti-ROCK2, anti-RLC, or anti-MYBPH antibodies.

In-vitro kinase assay

Purified GST-tagged RLC, GST-tagged ROCK1, and GST-tagged ROCK2 were incubated in phosphorylation buffer (25 mM Tris–HCl (pH 7.5), 5 mM $MgCl_2$, and 0.5 mM ATP) with or without purified His-tagged MYBPH at a final protein concentration of 0.1 μM for 1 h at 37°C. The reactions were analysed by SDS–PAGE, followed by western blot analysis with anti-phospho-RLC antibodies. For detection of phosphorylations, we used an *in-vitro* kinase assay, in which those proteins were incubated in kinase buffer containing 100 μm [γ-^{32}P]ATP (2 μCi), then resolved by SDS–

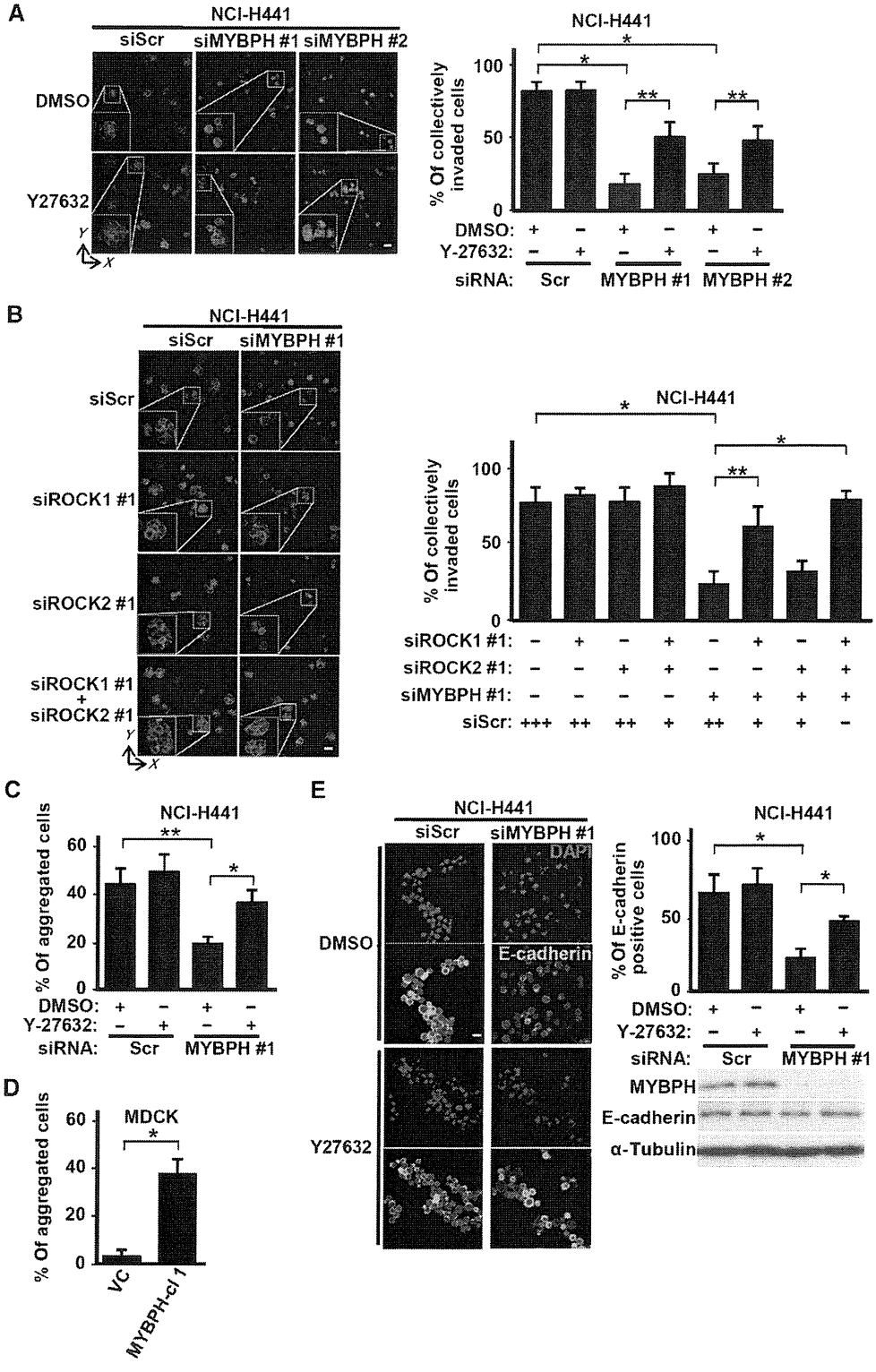

PAGE and stained with CBB reagents. Radiolabelled phosphoprotein bands were visualized by autoradiography of a dried gel.

Cell aggregation assay

Cells (1×10^6) were suspended in RPMI or DMEM medium supplemented with 10% FBS in 12-well plates pre-coated with 2% BSA (Roche), then cultured with horizontal rotation (75–100 r.p.m.) at 37°C for 30 min. Aggregation was fixed by adding 2% glutaraldehyde (Nacalai Tesque). The extent of aggregation ($\geqslant 5$ cells) was defined as the ratio of total particle number to initial cell number. Cells were then attached onto a slide glass using a *CYTOSPIN* device (2000 r.p.m., 5 min) followed by immunostaining, or were dissolved in 1 × SDS sample buffer, then subjected to western blot analysis. Cells with intense staining on the cell surface, as shown by MetaMorph software finding, were considered to be E-cadherin positive. Data shown represent three independent experiments, with >100 cells counted in each.

Statistical analysis

Statistical analyses of data presented in Figures 2B and 4F were performed using Fisher's exact test. For the other experiments, significance levels were determined by a *t*-test. All statistical analyses are performed in a two-sided manner.

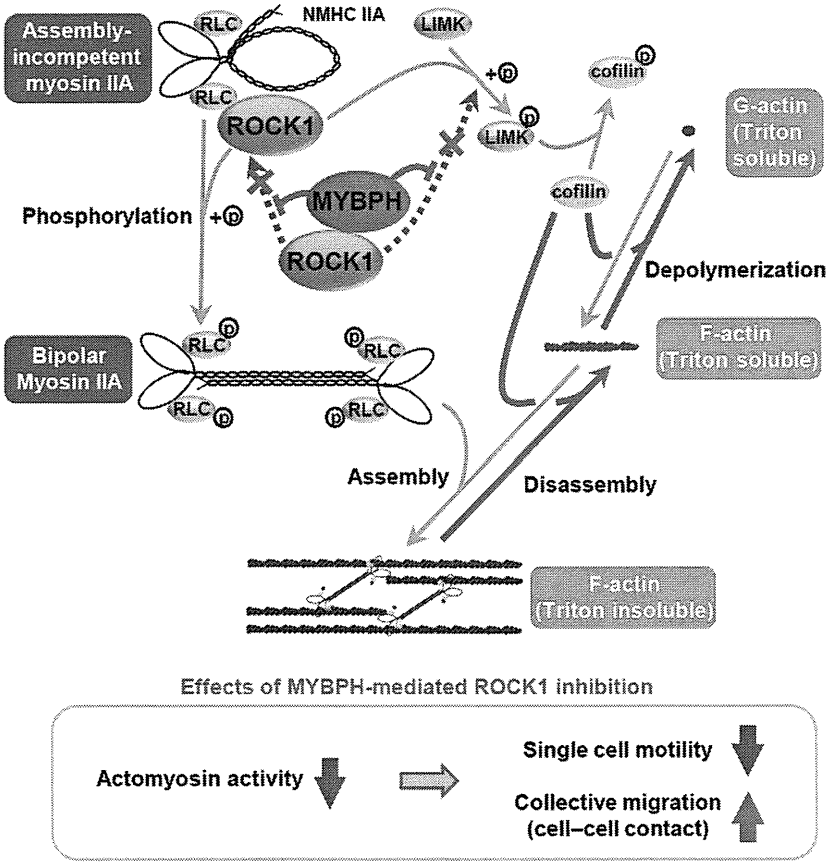

Figure 9 Schematic diagram demonstrating how MYBPH affects actomyosin organization through inhibition of ROCK1. RLC phosphorylation-mediated bipolar NM IIA formation, a prerequisite for actomyosin assembly, is disturbed by MYBPH via direct interaction with and negative regulation of ROCK1, which also leads to inhibition of the LIMK–cofilin pathway. Consequently, MYBPH inhibits ROCK1-driven actomyosin organization, which in turn reduces single cell motility and promotes collective cell migration.

Figure 8 MYBPH knockdown reduces cell–cell contact and collective cell migration. (**A**) Three-dimensional Matrigel invasion assay findings showing decreased collective cell migration by MYBPH knockdown and significant reversion by simultaneous Y-27632 treatment in NCI-H441 cells. Cells were visualized by actin staining (red). White bars indicate 50 μm. The proportions of cells with collective invasion were evaluated as in Figure 3D. Data shown represent three independent experiments. Bars, mean ± s.d.; $^*P<0.01$. (**B**) Three-dimensional Matrigel invasion assay findings showing decreased collective cell migration by MYBPH knockdown and significant reversion by simultaneous siROCK1 treatment in NCI-H441 cells. Cells were visualized by actin staining (red). White bars indicate 50 μm. The proportions of cells with collective invasion were evaluated as in Figure 3D. Data shown represent three independent experiments. Bars, mean ± s.d.; $^*P<0.01$.; $^{**}P<0.05$. siRNA concentrations: +, 40 nM; + +, 80 nM; + + +, 120 nM. (**C**) Cell aggregation assay findings showing that MYBPH knockdown decreased formation of cell aggregates and significant reversion by simultaneous Y-27632 treatment in NCI-H441 cells. The proportions of aggregated cells were evaluated as described in Materials and methods. Data shown represent three independent experiments. Bars, mean ± s.d.; $^*P<0.05$; $^{**}P<0.01$. (**D**) Cell aggregation assay findings showing increased numbers of cell aggregates in stable MYBPH transfectants of MDCK cells. Data shown represent three independent experiments. Bars, mean ± s.d.; $^*P<0.01$. (**E**) Immunofluorescent staining of E-cadherin in NCI-H441 cells subjected to cell aggregation assay. Cells were stained with anti-E-cadherin antibody (green) and DAPI (blue), which revealed decreased cell surface E-cadherin expression in NCI-H441 cells knocked down for MYBPH. Note that cell aggregation was also decreased by siMYBPH treatment and these phenotypic changes were significantly reverted when the cells were simultaneously treated with Y-27632. Western blot analysis findings showed negligible changes in total amounts of E-cadherin. Bar indicates 10 μm. Proportions of E-cadherin-positive cells were evaluated as described in Materials and methods. Data shown represent three independent experiments. Bars, mean ± s.d.; $^*P<0.01$. Figure source data can be found with the Supplementary data.